The Astrophysical Journal, 961:229 (18pp), 2024 February 1 https://doi.org/10.3847/1538-4357/ad11dc

Effect of Extinction on Quasar Luminosity Distances Determined from UV and X-Ray Flux Measurements

Michal Zajaček[1], Bożena Czerny[2], Narayan Khadka[3,4], Mary Loli Martínez-Aldama[5,6], Raj Prince[2], Swayamtrupta Panda[7,9], and Bharat Ratra[8]
[1] Department of Theoretical Physics and Astrophysics, Faculty of Science, Masaryk University, Kotlářská 2, 611 37 Brno, Czech Republic; zajacek@physics.muni.cz
[2] Center for Theoretical Physics, Polish Academy of Sciences, Al. Lotników 32/46, 02-668 Warsaw, Poland
[3] Department of Physics, Bellarmine University, 2001 Newburg Rd, Louisville, KY 40205, USA
[4] Department of Physics and Astronomy, Stony Brook University, Stony Brook, NY 11794, USA
[5] Astronomy Department, Universidad de Concepción, Casilla 160-C, Concepción 4030000, Chile
[6] Instituto de Física y Astronomía, Facultad de Ciencias, Universidad de Valparaíso, Gran Bretaña 1111, Playa Ancha, Valparaíso, Chile
[7] Laboratório Nacional de Astrofísica—MCTI, R. dos Estados Unidos, 154—Nações, Itajubá—MG, 37504-364, Brazil
[8] Department of Physics, Kansas State University, 116 Cardwell Hall, Manhattan, KS 66506, USA
Received 2023 August 23; revised 2023 November 16; accepted 2023 December 2; published 2024 January 31

Abstract

In Khadka et al., a sample of X-ray-detected reverberation-mapped quasars was presented and applied for the comparison of cosmological constraints inferred using two well-established relations in active galactic nuclei—the X-ray/UV luminosity (L_X–$L_{\rm UV}$) relation and the broad-line region radius–luminosity (R–L) relation. L_X–$L_{\rm UV}$ and R–L luminosity distances to the same quasars exhibit a distribution of their differences that is generally asymmetric and positively shifted for the six cosmological models we consider. We demonstrate that this behavior can be interpreted qualitatively as arising as a result of the dust extinction of UV/X-ray quasar emission. We show that the extinction always contributes to the nonzero difference between L_X–$L_{\rm UV}$-based and R–L-based luminosity distances and we derive a linear relationship between the X-ray/UV color index $E_{X-{\rm UV}}$ and the luminosity-distance difference, which also depends on the value of the L_X–$L_{\rm UV}$ relation slope. Taking into account the median and the peak values of the luminosity-distance difference distributions, the average X-ray/UV color index falls in the range of $\overline{E}_{X-{\rm UV}} = 0.03$–$0.28$ mag for the current sample of 58 sources. This amount of extinction is typical for the majority of quasars and can be attributed to the circumnuclear and interstellar media of host galaxies. After applying the standard hard X-ray and far-UV extinction cuts, heavily extincted sources are removed but overall the shift toward positive values persists. The effect of extinction on luminosity distances is more pronounced for the L_X–$L_{\rm UV}$ relation since the extinction of UV and X-ray emissions both contribute.

Unified Astronomy Thesaurus concepts: Cosmology (343); Cosmological parameters (339); Observational cosmology (1146); Active galaxies (17); Quasars (1319); Interstellar dust extinction (837)

1. Introduction

The spatially flat ΛCDM cosmological model (Peebles 1984) is largely consistent with most lower-redshift, $z \lesssim 2.3$, observations (Yu et al. 2018; eBOSS Collaboration 2021; Brout et al. 2022) as well as with high-redshift cosmic microwave background (CMB) data at $z \sim 1100$ (Planck Collaboration 2020). However, there are several potential tensions between flat ΛCDM parameter values inferred using different techniques (Abdalla et al. 2022; Moresco et al. 2022; Perivolaropoulos & Skara 2022; Hu & Wang 2023). These can be addressed by improving the accuracy and precision of established cosmological probe measurements, and also by looking for alternative cosmological probes, especially in the redshift range between nearby data and CMB data.

Active galactic nuclei (AGN), especially bright quasars (quasi-stellar objects (QSOs); Karas et al. 2021; Zajaček et al. 2023), appear to be promising alternative probes due to their broad redshift coverage, ranging from the nearby Universe ($z = 0.00106$ for NGC4395; Brum et al. 2019) to $z \approx 7.642$ (J0313-1806; Wang et al. 2021). For cosmological applications, so far three types of QSO data have been more widely utilized: (i) QSO angular size observations (Cao et al. 2017; Ryan et al. 2019; Cao et al. 2020, 2021a, 2021b; Lian et al. 2021; Cao et al. 2022b); (ii) data based on the nonlinear relation between QSO X-ray and UV luminosities, the L_X–$L_{\rm UV}$ relation (Risaliti & Lusso 2015, 2019; Khadka & Ratra 2020a, 2020b; Lusso et al. 2020; Khadka & Ratra 2021; Li et al. 2021; Colgáin et al. 2022; Dainotti et al. 2022; Hu & Wang 2022; Khadka & Ratra 2022; Petrosian et al. 2022; Rezaei et al. 2022; Khadka et al. 2023); and (iii) data based on the correlation between the rest-frame broad-line region (BLR) time delay and the monochromatic luminosity, the R–L relation (Panda et al. 2019a, 2019b; Martínez-Aldama et al. 2019; Khadka et al. 2021b, 2022a, 2022b; Czerny et al. 2021; Zajaček et al. 2021; Cao et al. 2022c, 2023; Cao & Ratra 2022; Panda 2022; Cao & Ratra 2023a; Czerny et al. 2023a; Panda & Marziani 2023). In addition to these methods, Elvis & Karovska (2002) suggested using angular diameters of the BLR to measure the cosmological constant Λ (also see Wang et al. 2020) and Collier et al. (1999) as well as Cackett et al. (2007) discussed the application of continuum reverberation mapping (RM) to measure the Hubble constant. Also, the H0LiCOW (H0 Lenses in COSMOGRAIL's Wellspring)

[9] CNPq Fellow.

program based on time delays between lensed images of QSOs has measured the Hubble constant (Birrer et al. 2020).

QSO standardization based on the L_X–$L_{\rm UV}$ relation and the constructed Hubble diagram has led to claims of strong cosmological constraints and tension with the ΛCDM model with the nonrelativistic matter density parameter $\Omega_{m0} \sim 0.3$ (Risaliti & Lusso 2019; Lusso et al. 2020). However, the analyses of Risaliti & Lusso (2019) and Lusso et al. (2020) were approximate and based on incorrect assumptions (Khadka & Ratra 2020a, 2020b; Banerjee et al. 2021; Khadka & Ratra 2021, 2022; Petrosian et al. 2022), i.e., cosmological parameters and L_X–$L_{\rm UV}$ relation parameters were constrained within the non-flat ΛCDM model; hence, the results were model dependent. The correct technique for the analysis of these data was developed by Khadka & Ratra (2020a) and here we outline it as follows: given the current quality of these data, one must use them to simultaneously determine the L_X–$L_{\rm UV}$ relation parameters and the cosmological model parameters, and one must also study a number of different cosmological models to determine whether the L_X–$L_{\rm UV}$ relation parameter values are independent of the assumed cosmological model. If the L_X–$L_{\rm UV}$ relation parameter values are independent of the assumed cosmological model, the QSOs are standardizable and the circularity problem is circumvented. We emphasize, however, that when correctly analyzed, the most recent Lusso et al. (2020) data compilation is not standardizable (Khadka & Ratra 2021, 2022) because the L_X–$L_{\rm UV}$ relation parameters depend on the assumed cosmological model as well as on redshift (Khadka & Ratra 2021, 2022). Khadka & Ratra (2022) discovered that the largest of the seven subsamples in the Lusso et al. (2020) QSO compilation, the Sloan Digital Sky Survey (SDSS)-4XMM one that contains about 2/3 of the total QSOs, has an L_X–$L_{\rm UV}$ relation that depends on the cosmological model and on redshift and is the main source of the problem with the Lusso et al. (2020) data.

On the other hand, the BLR R–L relation parameters generally appear independent of the adopted cosmological model (Khadka et al. 2021b, 2022a, 2022b; Cao et al. 2022c). Cosmological constraints are weak, but for Mg II (at 2798 Å in the rest frame) and C IV QSOs (at 1549 Å in the rest frame) they are consistent with those from better established probes (Khadka et al. 2022b; Cao et al. 2022c). However, there is a 2σ tension between the constraints given by lower-redshift Hβ QSOs (at 4861 Å in the rest frame) and those from the better established probes (Khadka et al. 2022a). The Hβ QSO sample yields weak cosmological constraints with a preference for decelerated cosmological expansion. This tension, and possible systematic issues, related to Hβ QSOs will need to be addressed when more reverberation-mapped QSOs are available, e.g., from the upcoming Vera C. Rubin telescope and its Legacy Survey of Space and Time (LSST; see, e.g., Panda et al. 2019a; Ivezić et al. 2019; Czerny et al. 2023b) and the SDSS-V black hole Mapper (Almeida et al. 2023).

In summary, both the L_X–$L_{\rm UV}$ relation and R–L relation data provide cosmological constraints, which is encouraging, but they have systematic problems that require further study. To uncover the systematic issues we looked for a sample of X-ray-detected quasars that have been reverberation mapped in the UV domain using the Mg II line. For such a sample, in principle, both L_X–$L_{\rm UV}$ and R–L relations should be applicable. To this goal, we provided a sample of 58 X-ray-detected reverberation-mapped Mg II QSOs in Khadka et al. (2023), from which we measured both the L_X–$L_{\rm UV}$ relation and the R–L relation parameter values that are consistent with values measured using larger samples. The sample was quite limited but we stress that for each of the sources we could determine the luminosity distance from these two methods independently. The goal was to compare cosmological constraints inferred from the QSOs for both of these relations not just in the overall statistical study of two independent samples but for the same sample. Using six cosmological models, we found that both R–L and L_X–$L_{\rm UV}$ relations are standardizable. The main result of this study was that while the R–L relation measurements favored a smaller Ω_{m0} value consistent with the $\Omega_{m0} \sim 0.3$ value measured using better established cosmological probes, the L_X–$L_{\rm UV}$ relation measurements favored a value of Ω_{m0} larger than that inferred from the better established cosmological probes.

In Khadka et al. (2023), we showed that this is in agreement with the tendency for luminosity distances based on L_X–$L_{\rm UV}$ relation data to have a mean value smaller than luminosity distances based on R–L relation data for the same QSOs. The median L_X–$L_{\rm UV}$ relation luminosity-distance values, on the other hand, are mostly larger except for the flat and non-flat XCDM models. We note that these results are based on the distribution of the luminosity-distance difference ($\log D_{L,R-L} - \log D_{L,L_X-L_{\rm UV}}$) normalized by the square root of the quadratic sum of the corresponding uncertainties.

Here we revisit the nonzero median (mean) of the difference in the luminosity distances based on the L_X–$L_{\rm UV}$ relation and R–L relation data sets. It is expected that, in the absence of systematic effects, the median (mean) of the distance-difference distribution should vanish within uncertainties since we construct the distribution from the same sample of sources and the luminosity distance to a particular source must be the same for both methods. The offset from zero hints at a systematic effect in one or both data sets and demands further analysis.

We propose that the offset in the $\Delta \log D_L \equiv \log D_{L,L_X-L_{\rm UV}} - \log D_{L,R-L}$ distribution may be attributed to the extinction (absorption and scattering) of UV and X-ray photons along the line of sight. Since the extinction curve generally increases from the UV (2500 Å) to the soft X-ray bands (2 keV), we evaluate the differential extinction or the difference in optical depth between the X-ray and UV bands, $\tau_X - \tau_{\rm UV}$. Specifically, we derive a simple analytical relation between $\tau_X - \tau_{\rm UV}$ and the slope γ' of the L_X–$L_{\rm UV}$ relation as well as the luminosity-distance difference $\Delta \log D_L$, i.e., $\tau_X - \tau_{\rm UV} \simeq 4.6(\gamma' - 1)\Delta \log D_L$. This way the mean differential extinction effect, or the X-ray/UV color index, can be directly inferred for the current sample of 58 X-ray reverberation-mapped QSOs as well as any future sample of such sources.

We show that the asymmetry and the positive shift of $\Delta \log D_{\rm L}$ distributions for all the considered cosmological models, including the flat ΛCDM model, with prevailing positive medians, can be explained by a mild extinction of the UV and X-ray flux densities from QSOs. From all the median and the peak values of the $\Delta \log D_L$ distributions, the X-ray/UV color index falls in the range of ∼0.03–0.28 mag for the sample of 58 X-ray detected, reverberation-mapped sources (Khadka et al. 2023). We demonstrate that this amount of extinction is typical for the majority of QSOs, originates in the circumnuclear and interstellar media of host galaxies

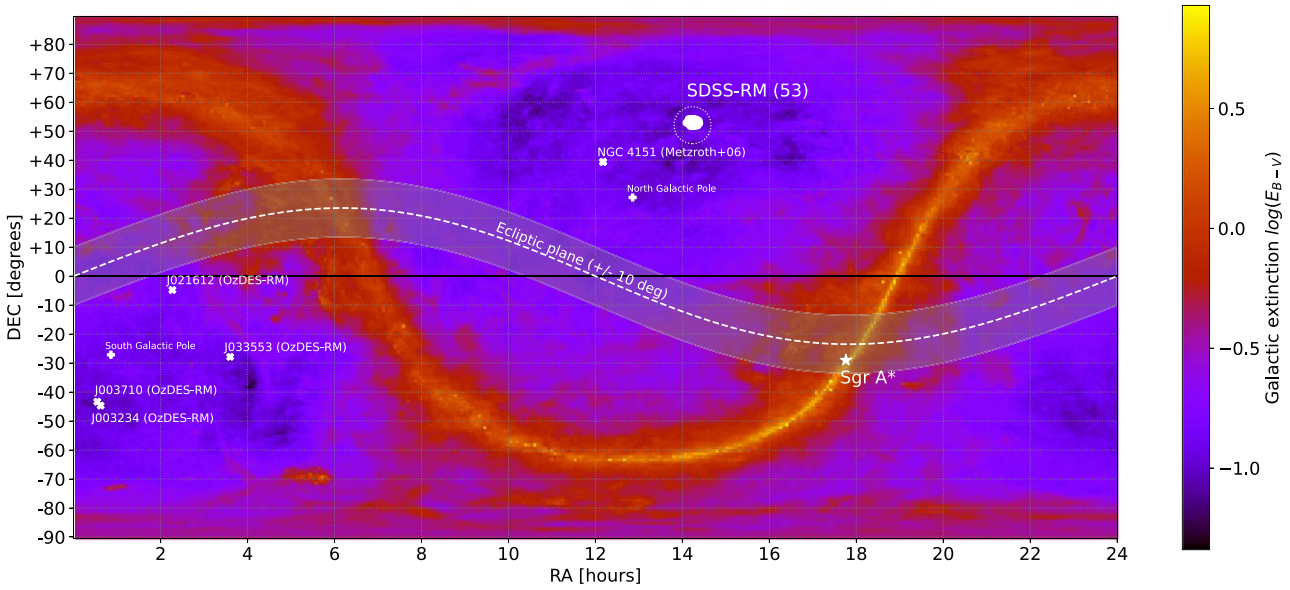

Figure 1. The position of the sample of 58 X-rays detected reverberation-mapped sources on the sky. Right ascension (R.A. expressed in hours) is along the x-axis, while decl. (decl. expressed in degrees) is along the y-axis. The white-dotted circle in the northern hemisphere denotes the sample of 53 SDSS-RM sources (Shen et al. 2016, 2019; Homayouni et al. 2020), while the five remaining sources (Metzroth et al. 2006; Yu et al. 2021) are more scattered to the south. The figure also shows the dust extinction map of the Milky Way (red-orange band) color coded using the logarithm of the $(B-V)$ color index E_{B-V} according to Schlegel et al. (1998). The position of the Galactic center (Sgr A*) is marked by a white star, while the north and the south Galactic poles are depicted by plus signs. The ecliptic plane and the surrounding band of $\pm$ 10° are represented by the white-dashed line and the gray-shaded area, respectively.

(Czerny et al. 2004), and is only slightly alleviated by standard hard X-ray and far-UV extinction cuts (Lusso et al. 2020). Since the L_X–$L_{\rm UV}$ relation employs both UV and X-ray flux density measurements, it turns out to be more affected by extinction, which can address some of the previously mentioned problems with its standardization.

Our paper is structured as follows. In Section 2, we describe the characteristics of the data set of X-ray reverberation-mapped QSOs. In Section 3, we summarize the calculation method for luminosity distances and the different cosmological models we utilize. Subsequently, in Section 4, we derive the relation between the X-ray and UV optical depth difference (color index) and the luminosity-distance difference. Our main results are presented in Section 5. We provide an additional discussion of the source selection and our results in Section 6 and conclude in Section 7.

The reader may also find additional derivations of luminosity distances, including the extinction law in Appendix A, whereas the distributions related to the luminosity-distance difference formula are presented in Appendix B. Additional distributions of the X-ray/UV color index for different cosmological models are shown in Appendix C and the detailed investigation of reddening using SDSS magnitudes is presented in Appendix D.

2. Data Description

Our sample consists of 58 sources that were both (i) reverberation mapped using UV continuum and Mg II emission-line light curves, and (ii) X-ray detected at 2 keV. In this regard, the sample is complete, and due to its small size, we are not imposing further selection criteria unless stated otherwise. There are altogether 59 measurements of BLR time delays since the time delay for NGC 4151 was measured twice (Metzroth et al. 2006). The sample is described in detail in Khadka et al. (2023), and we list the main observables, i.e., the redshift z, the rest-frame Mg II time delay τ, 2 keV flux density per frequency F_X, 2500 Å flux density per frequency $F_{\rm UV}$, and 3000 Å flux density F_{3000}, in Appendix A of Khadka et al. (2023). The sample consists of 53 sources from the SDSS-RM program (Shen et al. 2016, 2019; Homayouni et al. 2020), NGC 4151 (Metzroth et al. 2006), and four sources from the OzDES RM program (Yu et al. 2021). These sources are also detected in the X-ray domain and are listed in the XMM-Newton X-ray source catalog (4XMMDR11). The sample position on the sky to the Galactic plane and the Galactic center (Sgr A*; Eckart et al. 2017) is shown in Figure 1, which is color coded using the decadic logarithm of the $(B-V)$ color index $\log E_{B-V}$ according to Schlegel et al. (1998).

We summarize the main properties of the main sample in Table 1. In Khadka et al. (2023), we also estimated the α_{OX} parameter, finding that our sample is not heavily obscured. An alternative verification that the Mg II quasars are not intrinsically obscured sources (or red quasars) is presented in Appendix D using *ugriz* magnitudes from the SDSS database.

In addition, we analyze a subsample of 21 sources that meet the hard X-ray index and far-UV slope criteria of Lusso et al. (2020).[10] The selection methodology and the subsample were described in detail in Khadka et al. (2023).[11] The properties of the subsample are also described in Table 1.

3. Cosmological Models and Parameters

The application of these QSO observations in cosmology depends on the empirical measurement of the QSO luminosity distances. This requires the assumption of a cosmological model. However, to determine whether or not the QSOs are

[10] The hard X-ray photon index should lie between 1.7 and 2.8 and the far-UV spectral slope should lie between −0.7 and 1.5 (Lusso et al. 2020). The extinction cuts are applied to the sources that are outside these limits.

[11] Using the source identification (ID) of Khadka et al. (2023; see their Appendix A), the IDs of the sources are the following: 18, 28, 44, 118, 159, 185, 260, 280, 301, 303, 338, 440, 449, 459, 522, 588, 675, J141214, J141018, J141650, and J141644.

Table 1
Selected Properties of the Main Sample of X-Ray Detected Reverberation-mapped QSOs and the Subsample of 21 Sources

Property	Main Sample	Subsample
Source number	58	21
Redshift range	(0.0041, 1.686)	(0.418, 1.587)
Redshift (16th, 50th, 84th) percentiles	(0.527, 0.990, 1.454)	(0.4810, 0.919, 1.3394)
2 keV luminosity range [erg s^{-1}]	(1.9×10^{41}, 6.1×10^{44})	(1.6×10^{43}, 1.5×10^{44})
2 keV luminosity median [erg s^{-1}]	4.4×10^{43}	4.8×10^{43}
2500 Å luminosity range [erg s^{-1}]	(1.2×10^{43}, 1.3×10^{46})	(5.9×10^{43}, 4.8×10^{45})
2500 Å luminosity median [erg s^{-1}]	9.3×10^{44}	9.5×10^{44}
Mg II time delay range [days]	(5.3, 387.9)	(17.2, 387.9)
Mg II time delay median [days]	92.0	99.1

Note. The luminosities are computed for the flat ΛCDM model with $\Omega_{m0} = 0.3$ and $H_0 = 70$ km s^{-1} Mpc^{-1}. Mg II time delays are expressed in the rest frames of the sources. See Section 2 for the details of the subsample of 21 sources.

standardizable requires that we study them in several different cosmological models to see whether or not the empirical correlation relation used to determine their luminosities is independent of the assumed cosmological model (Khadka & Ratra 2020c). In this paper, we use three spatially flat and three spatially non-flat[12] cosmological models to determine QSO luminosity distances. In any cosmological model, the luminosity distance can be computed as a function of redshift (z) and cosmological parameters (p) in the following way:

$$D_L(z, p) = \begin{cases} \frac{c(1+z)}{H_0\sqrt{\Omega_{k0}}} \sinh\left[\frac{H_0\sqrt{\Omega_{k0}}}{c} D_C(z, p)\right] & \text{if } \Omega_{k0} > 0, \\ (1+z) D_C(z, p) & \text{if } \Omega_{k0} = 0, \\ \frac{c(1+z)}{H_0\sqrt{|\Omega_{k0}|}} \sin\left[\frac{H_0\sqrt{|\Omega_{k0}|}}{c} D_C(z, p)\right] & \text{if } \Omega_{k0} < 0. \end{cases} \quad (1)$$

Here c is the speed of light, H_0 is the Hubble constant, Ω_{k0} is the current value of the spatial curvature energy density parameter, and $D_C(z, p)$ is the comoving distance. $D_C(z, p)$ is computed as a function of z and p for a given cosmological model as follows:

$$D_C(z, p) = c \int_0^z \frac{dz'}{H(z', p)}, \quad (2)$$

where $H(z, p)$ is the Hubble parameter that is given next for the six cosmological models we use in this paper.

In a compact form, the Hubble parameter for all the six models (spatially flat/non-flat ΛCDM model, XCDM parameterization, and ϕCDM model) can be written as

$$H(z) = H_0\sqrt{\Omega_{m0}(1+z)^3 + \Omega_{k0}(1+z)^2 + \Omega_{DE}(z)}, \quad (3)$$

where Ω_{k0} vanishes in the spatially flat models. For the ΛCDM models and XCDM parameterizations, $\Omega_{DE}(z) = \Omega_{DE0}(1+z)^{1+\omega_X}$, where Ω_{DE0} is the current value of the dark energy density parameter and ω_X is the dark energy equation of state parameter. For the ΛCDM models $\omega_X = -1$ and the XCDM parameterizations, ω_X, is a free parameter to be determined from observational data. For the ϕCDM models (Peebles & Ratra 1988; Ratra & Peebles 1988; Pavlov et al. 2013), $\Omega_{DE}(z) = \Omega_\phi(z, \alpha)$ can be obtained by solving the equations of motion of a spatially homogeneous scalar field model numerically. Here α is a positive parameter characterizing the inverse power-law potential energy density of the dynamical dark energy scalar field (ϕ) and can be constrained by using observational data.[13]

To determine QSO luminosity distances using empirical correlation relations, in particular, those expressed by Equations (4) and (6) below, we perform a likelihood analysis of predicted luminosity distances in a given cosmological model using Equation (1) and the observational luminosity distances obtained from Equations (5)–(7) below. This allows us to measure the nuisance parameters involved in the correlation relation (and check whether they are independent of cosmological model parameters), and that ultimately leads us to the determination of the QSO luminosity distances. For a detailed description of the computational method and the determination of QSO luminosity distances used in this paper, see Khadka et al. (2023).

4. UV and X-Ray Extinction and Luminosity Distances

The source intrinsic UV and X-ray flux densities (per frequency) at 2500 Å and 2 keV are $F_{\rm UV,int}$ and $F_{\rm X,int}$, respectively, and originate in the very central parts of galaxies during the accretion process and as such are assumed to be unaffected by dust at the place of their origin. The corresponding luminosities are calculated as $L_{\rm UV,int} = 4\pi D_L^2 F_{\rm UV,\,int}$ and $L_{\rm X,int} = 4\pi D_L^2 F_{\rm X,int}$, where D_L is the luminosity distance of a given QSO.

For the R–L relation, the corresponding UV luminosity is expressed at 3000 Å, $L_{3000,\rm int} = 4\pi\ D_L^2 F_{3000,\nu}\nu_{3000} = 4\pi\ D_L^2 F_{\rm UV,int}(2500/3000)^{\alpha_\nu}\nu_{3000}$, where $\alpha_\nu \simeq -0.45$ is the mean QSO continuum slope in the frequency domain, $F_\nu \propto \nu^{\alpha_\nu}$ (Vanden Berk et al. 2001) and ν_{3000} is the frequency corresponding to 3000 Å. Since the relation between the mean radius of the BLR region R and the corresponding time delay τ in the rest frame of the source is given by the light–travel relation, $R = c\tau$,

[12] For discussions of the constraints on spatial curvature see Rana et al. (2017), Ooba et al. (2018a), Park & Ratra (2019a), DES Collaboration (2019), Efstathiou & Gratton (2020), Di Valentino et al. (2021), Khadka et al. (2021a), Dhawan et al. (2021), Vagnozzi et al. (2021a, 2021b), Renzi et al. (2022), Geng et al. (2022), Cao et al. (2022a), Mukherjee & Banerjee (2022), Glanville et al. (2022), Wu et al. (2023), de Cruz Pérez et al. (2023), Dahiya & Jain (2023), Stevens et al. (2023), Favale et al. (2023, and references therein).

[13] For discussions of the constraints on the ϕCDM model see Zhai et al. (2017), Ooba et al. (2018b, 2019), Park & Ratra (2018, 2019b, 2020), Solà Peracaula et al. (2019), Singh et al. (2019), Ureña-López & Roy (2020), Sinha & Banerjee (2021), Xu et al. (2022), de Cruz Perez et al. (2021), Jesus et al. (2022), Adil et al. (2023), Dong et al. (2023), Van Raamsdonk & Waddell (2023), Cao & Ratra (2023b, and references therein).

the R–L relation can be expressed in the form using τ instead of R,

$$\log\left(\frac{\tau}{\text{days}}\right) = \beta + \gamma \log\left(\frac{L_{3000,\text{int}}}{10^{\eta}\ \text{erg s}^{-1}}\right), \tag{4}$$

where γ, β, and η represent the slope, intercept, and normalization coefficients, respectively. From Equation (4), we can derive an expression for the luminosity distance $D_{L,R-L}$ as a function of τ, $F_{\text{UV, int}}$, and the coefficients of the R–L relation

$$\log D_{L,R-L} = \frac{1}{2\gamma}\{\log\tau - \beta - \gamma[\log(4\pi) + \log F_{\text{UV, int}} + 15.04 - \eta]\}, \tag{5}$$

where the term 15.04 results from the evaluation of $\log[(2500/3000)^{\alpha_\nu}\nu_{3000}]$. The L_X–L_{UV} relation considering the intrinsic X-ray and UV luminosities of the sources $L_{\text{X,int}}$ and $L_{\text{UV,int}}$ located at the luminosity distance $D_{L,L_X-L_{\text{UV}}}$ can be expressed as

$$\log\left(\frac{L_{\text{X,int}}}{\text{erg s}^{-1}\,\text{Hz}^{-1}}\right) = \beta' + \gamma' \log\left(\frac{L_{\text{UV,int}}}{10^{\eta'}\ \text{erg s}^{-1}\text{Hz}^{-1}}\right), \tag{6}$$

where β', γ', and η' denote quantities analogous to those in Equation (4). The luminosity distance, $D_{L,L_X-L_{\text{UV}}}$, inferred from the L_X–L_{UV} relation given in Equation (6) is

$$\log D_{L,L_X-L_{\text{UV}}} = \frac{1}{2(1-\gamma')}[\beta' + (\gamma'-1)\log(4\pi) + \gamma'(\log F_{\text{UV, int}} - \eta') - \log F_{\text{X,int}}]. \tag{7}$$

Taking into account just the intrinsic UV and X-ray flux densities, we can evaluate the luminosity-distance difference, $\Delta\log D_L$, as

$$(\log D_{L,L_X-L_{\text{UV}}} - \log D_{L,R-L})_{\text{int}} = \delta + \frac{\log F_{\text{UV, int}} - \log F_{\text{X,int}}}{2(1-\gamma')}, \tag{8}$$

where the factor δ is a function of γ, β, γ', β', and τ,

$$\delta = \frac{\beta - \log\tau}{2\gamma} + \frac{\beta' - \gamma'\eta'}{2(1-\gamma')} + 7.52 - \frac{\eta}{2}, \tag{9}$$

where the term 7.52 results from the evaluation of $0.5\log[(2500/3000)^{\alpha_\nu}\nu_{3000}]$.

In the following, we adopt the assumption that, in the absence of a systematic effect, the luminosity-distance difference for a given source, or the statistical mean (median) of the luminosity-distance differences for a source sample, vanish, i.e., $(\Delta\log D_L)_{\text{int}} \equiv 0$; hence, $\delta + (\log F_{\text{UV, int}} - \log F_{\text{X,int}})/[2(1-\gamma')] = 0$. However, during the propagation of light through the circumnuclear and interstellar medium of the host galaxy, both UV and X-ray photons are absorbed and scattered with wavelength-dependent optical depths τ_{UV} and τ_X, respectively. The observed flux densities are therefore attenuated following the exponential law, $F_{\text{UV}} = F_{\text{UV, int}}\exp(-\tau_{\text{UV}})$ and $F_X = F_{\text{X,int}}\exp(-\tau_X)$. Hence, the resulting luminosity-distance difference under the influence of extinction in both the UV and X-ray domains is

$$\begin{aligned}(\Delta\log D_{\text{L}})_{\text{ext}} &= \delta + \frac{\log F_{\text{UV, int}} - \log F_{\text{X,int}}}{2(1-\gamma')} + \frac{(\tau_X - \tau_{\text{UV}})\log e}{2(1-\gamma')} \\ &= \frac{(\tau_X - \tau_{\text{UV}})\log e}{2(1-\gamma')},\end{aligned} \tag{10}$$

where the second equation follows because the sum of the first two terms on the right-hand side of the first part of Equation (10) is intrinsically zero. In Equation (10), $\log e$ denotes the decadic logarithm of Euler's number, i.e., $\log e \simeq 0.434$. We outline a more detailed, step-by-step derivation of Equation (10) in Appendix A. The relation among the distributions of δ, $(\log F_{\text{UV}} - \log F_X)/[2(1-\gamma')]$, and $\Delta\log D_L$ for our sample is discussed in Appendix B.

Consequently, the optical depth difference $\tau_X - \tau_{\text{UV}}$ can be expressed as a function of the luminosity-distance difference and the slope γ' of the L_X–L_{UV} relation

$$\tau_X - \tau_{\text{UV}} = \frac{2(1-\gamma')}{\log e}(\Delta\log D_L)_{\text{ext}}. \tag{11}$$

The extinction in magnitude at a given wavelength is directly proportional to the optical depth, $A_\lambda = 1.086\tau_\lambda$. Hence, we can express the X-ray/UV color excess as

$$E_{X-\text{UV}} \equiv A_X - A_{\text{UV}} \simeq 5.001(1-\gamma')\langle(\Delta\log D_L)_{\text{ext}}\rangle, \tag{12}$$

where the angular brackets represent the median/mean/peak value of the luminosity-distance difference for a given population of QSOs.

5. Results

In Khadka et al. (2023), we simultaneously measured the R–L or L_X–L_{UV} relation parameters and the cosmological model parameters for six different cosmological models—flat and non-flat ΛCDM, XCDM, and ϕCDM. Based on the cosmological parameter values, we computed the R–L-based and L_X–L_{UV}-based luminosity distances, $D_{L,R-L}$ and $D_{L,L_X-L_{\text{UV}}}$, respectively. In Figure 2 we show the distributions of $\Delta\log D_{\text{L}}$. The plot shows that the difference between the luminosity distances can be positive or negative. If extinction plays the dominant role in measurement accuracy, the difference should always be positive. The presence of negative values implies that other measurement errors dominate. On the other hand, if no extinction effect is present, the mean/median values should be consistent with zero. Establishing the systematic shift is important, particularly from the point of view of future measurements coming from very large samples, when the stochastic net error for the entire sample will become small but the systematic shift will persist. With this aim, we concentrate on tracing this systematic shift in the present sample.

In comparison with Khadka et al. (2023), here we construct distributions of non-normalized luminosity-distance differences, from which $E_{X-\text{UV}}$ can be inferred using Equation (12). The normalized luminosity-distance distributions computed in Khadka et al. (2023) are appropriate for comparing the R–L-based and L_X–L_{UV}-based luminosity distances for each source. For the graphical representation in Figure 2, we binned $\Delta\log D_L$ using Knuth's rule (Knuth 2006).

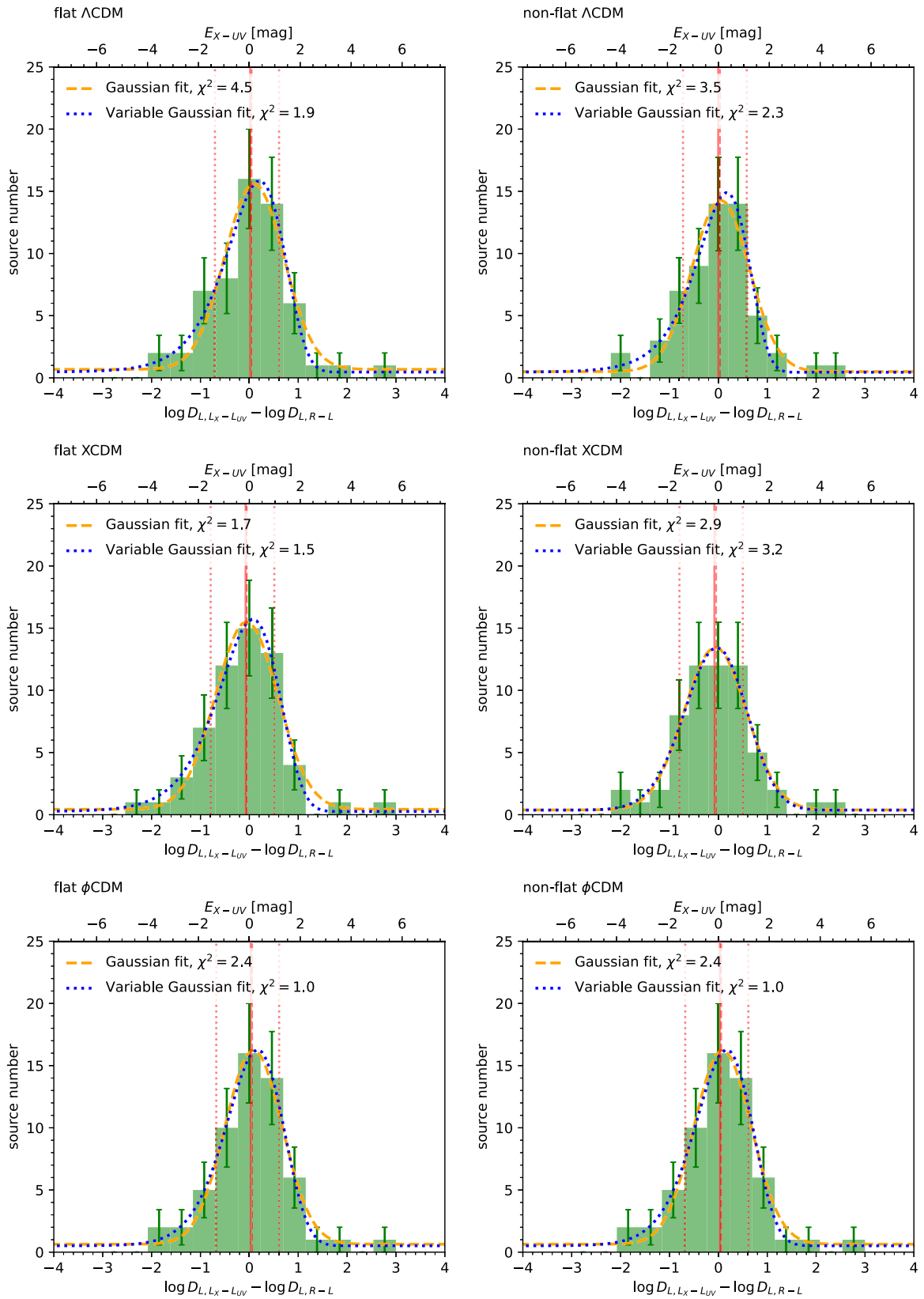

Figure 2. Distributions of the quasar luminosity-distance differences $\Delta \log D_L = \log D_{L,L_{X-L_{UV}}} - \log D_{L,R-L}$ for 58 sources for flat and non-flat ΛCDM, XCDM, and ϕCDM cosmological models (from top to bottom row). The X-ray/UV color index $E_{X-UV} = 5.001(1-\gamma')\Delta \log D_L$ is enumerated along the top x-axis in each panel. Solid red vertical lines indicate the mean difference, red-dashed vertical lines indicate the median difference, and red-dotted vertical lines denote the 16th and 84th percentiles. The bin width is determined based on the Knuth binning algorithm and the source number uncertainties for each bin are $\sigma_{y,i} = \sqrt{N_i}$, where N_i is the number of points in each bin. The orange-dashed line depicts the best-fit Gaussian function and the blue-dotted line shows the best-fit variable Gaussian function.

Table 2
Characteristics of the Distributions $\Delta \log D_L = \log D_{L,L_X-L_{UV}} - \log D_{L,R-L}$ for the Six Cosmological Models Considered in This Paper

Model	Median	16th Percentile	84th Percentile	Mean	Skewness	Fisher's Kurtosis	Kurtosis Test	K-S test
Flat ΛCDM	0.0423	−0.7036	0.6080	0.0167	0.2369	1.7366	2.1136, $p = 0.035$	0.0000, $p = 1.0000$
Non-flat ΛCDM	0.0310	−0.7229	0.5806	−0.0030	0.2194	1.7271	2.1068, $p = 0.035$	0.0690, $p = 0.9993$
Flat XCDM	−0.0539	−0.7911	0.5106	−0.0768	0.2418	1.7391	2.1154, $p = 0.034$	0.1034, $p = 0.9192$
Non-flat XCDM	−0.0490	−0.7969	0.5003	−0.0812	0.2228	1.7290	2.1082, $p = 0.035$	0.1034, $p = 0.9192$
Flat ϕCDM	0.0534	−0.6766	0.6097	0.0293	0.2390	1.7376	2.1144, $p = 0.034$	0.0345, $p = 1.0000$
Non-flat ϕCDM	0.0556	−0.6780	0.6128	0.0307	0.2375	1.7369	2.1139, $p = 0.035$	0.0517, $p = 1.0000$
Flat ΛCDM—21	0.1869	−0.4825	0.5173	0.0114	−0.8175	0.2430	0.4899, $p = 0.624$	0.1552, $p = 0.7855$

Note. The distributions are graphically depicted in Figure 2. From the left to the right columns, we list the distribution median, 16th and 84th percentiles, mean, skewness, and Fisher's kurtosis parameters (both corrected for statistical bias), the kurtosis test, and the K-S test statistic including the corresponding p-values.

Table 3
Parameters of the X-Ray/UV Extinction E_{X-UV} in Magnitude for Six Cosmological Models Inferred Using the Variable Gaussian Function That Fits the E_{X-UV} Distributions Better than a Normal Gaussian Function

Model (1)	γ' (2)	E_{X-UV} (mag) (median) (3)	E_{X-UV} (mag) (peak) (4)	σ_+ (mag) (5)	σ_- (mag) (6)
Flat ΛCDM	0.616 ± 0.074	0.081	0.29 ± 0.13	1.06 ± 0.11	1.29 ± 0.12
Non-flat ΛCDM	0.609 ± 0.073	0.061	0.31 ± 0.10	0.95 ± 0.09	1.25 ± 0.10
Flat XCDM	0.614 ± 0.075	−0.104	0.17 ± 0.13	1.02 ± 0.12	1.29 ± 0.13
Non-flat XCDM	0.608 ± 0.075	−0.096	0.20 ± 0.11	0.89 ± 0.10	1.20 ± 0.11
Flat ϕCDM	0.609 ± 0.073	0.104	0.34 ± 0.11	1.03 ± 0.10	1.28 ± 0.11
Non-flat ϕCDM	0.610 ± 0.073	0.108	0.34 ± 0.11	1.03 ± 0.10	1.28 ± 0.11
Flat ΛCDM—21	0.610 ± 0.100	0.364	0.50 ± 0.12	0.82 ± 0.09	1.20 ± 0.13

Note. We transform the luminosity-distance difference $\Delta \log D_L$ to the color excess E_{X-UV} using Equation (12) with the best-fit slope of the L_X–L_{UV} relation (column (2)) adopted from Khadka et al. (2023). Columns (3)–(6) (from the left to the right) list the E_{X-UV} median and peak values, and the standard deviations to the positive and the negative sides of the distributions, respectively. The quoted errors are the errors of the fit of the variable Gaussian function to the E_{X-UV} histograms

The uncertainty in the number of sources falling into the bin is estimated as $\sigma_{y,i} = \sqrt{N_i}$.

The distributions of the luminosity-distance differences have several common characteristics. At first glance, the peak of each distribution is shifted to the positive side, which hints at positive values of $\tau_X - \tau_{UV,}$ and hence, also E_{X-UV}. We summarize the main characteristics, specifically the median distribution, 16th and 84th percentiles, mean, skewness, Fisher's kurtosis, kurtosis test, and the Kolmogorov–Smirnov (K-S) test statistic, in Table 2. More specifically, for calculating the distribution skewness, we correct for the statistical bias and use the Fisher–Pearson standardized moment $\sqrt{N(N-1)}/(N-2)m_3/m_2^{3/2}$, where N is the sample size and m_2 and m_3 denote the second and the third central moments, respectively. All of the distributions are positively skewed, which is caused by the presence of tails on the positive side. For four out of six models, the median is positive; it is negative for the flat and non-flat XCDM models. The mean value is positive for the flat ΛCDM, flat, and non-flat ϕCDM models, while for the other cosmological models, it is negative. Since the mean is more sensitive to the outliers in the distribution tails, we consider the median values to be more representative of the quasar sample. Fisher's kurtosis, which is also corrected for the statistical bias, is greater than zero, which implies a heavier tail than for the normal distribution. We verify the deviation from the normal distribution by performing the kurtosis test, whose z-scores and the corresponding p-values confirm the deviation. The two-sample K-S test is applied between each model and the flat ΛCDM model. All of the K-S p-values are close to 1; hence, the null hypothesis that the $\Delta \log D_L$ distributions are drawn from the same underlying distribution as the one for the flat ΛCDM model is valid.

Furthermore, we analyze the $\Delta \log D_L$ distributions in Figure 2 by fitting a Gaussian function and a variable Gaussian function to them.[14] The comparison of the fits based on the χ^2 value shows that the variable Gaussian function fits the distributions better, with the peak value shifted to the positive side and with $\sigma_- > \sigma_+$, i.e., the distributions are asymmetric to the peak. Qualitatively the same behavior is traced for the distributions of the X-ray/UV color index E_{X-UV} (in magnitude), which is calculated using Equation (12) and its value is greater than the luminosity-distance offset by about a factor of 2. We show the corresponding histograms binned according to Knuth's rule, including the Gaussian and the variable Gaussian fits, for all the flat and non-flat ΛCDM, XCDM, and ϕCDM cosmological models in Figure 9 in Appendix C. In Figure 9, the distribution means are represented by red solid vertical lines, medians are represented by red vertical dashed lines, and the 16th and 84th percentiles are shown with red vertical dotted lines. The basic statistical properties of these distributions, specifically the E_{X-UV} median and peak values, the right and the left standard deviations, σ_+ and σ_-, respectively, are summarized in Table 3. For all the cosmological models, we obtain $\sigma_+ < \sigma_-$, which implies a significant asymmetry. The median values are predominantly positive (except for the flat and non-flat XCDM models), with an average value of

[14] For the variable Gaussian function, we use the form according to Barlow (2004). The variable Gaussian function is introduced as $G_{var} = a \exp(-(x - x_0)^2/[2\sigma(x)]) + b$, where $\sigma(x) = \sigma_1 + \sigma_2(x - x_0)$, $\sigma_1 = (2\sigma_+\sigma_-)/(\sigma_+ - \sigma_-)$, and $\sigma_2 = (\sigma_+ - \sigma_-)/(\sigma_+ + \sigma_-)$.

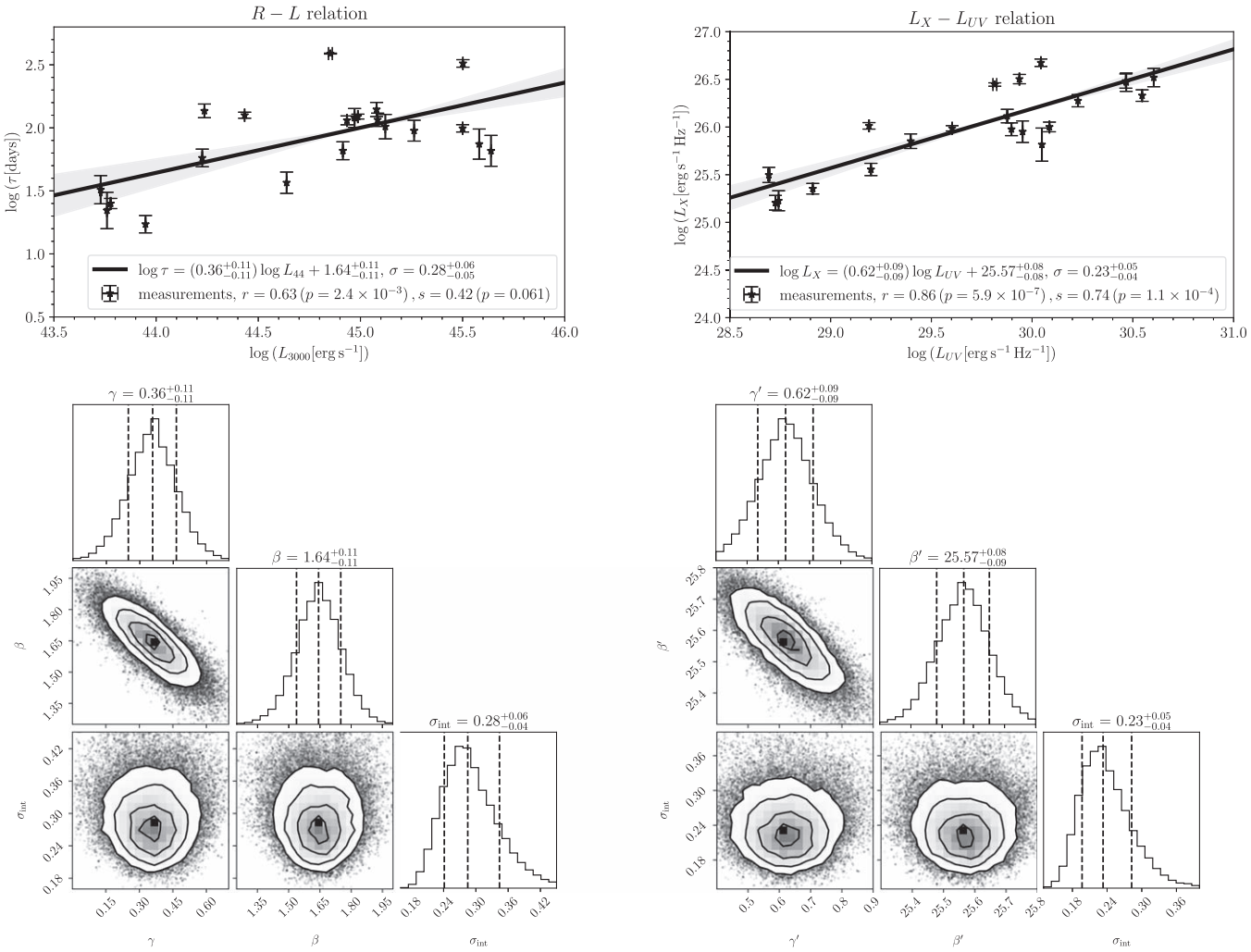

Figure 3. *R–L* and L_X–$L_{\rm UV}$ relations in the flat ΛCDM model ($\Omega_{m0} = 0.3$) in the left and the right panels, respectively, for the subsample of 21 sources. The top row depicts the measurements alongside the best-fit relations, including the intrinsic scatter σ, while the bottom row shows the likelihood distributions for the slopes γ and γ', the intercepts β and β', as well as the intrinsic scatter $\sigma_{\rm int}$ for the corresponding relations.

Table 4
Marginalized One-dimensional Best-fit Parameters with 1σ Confidence Intervals for the 21 L_X–$L_{\rm UV}$ and *R–L* QSOs in the Flat ΛCDM Model

Model	Data	Ω_{m0}	$\sigma_{\rm int}$	β, β'	γ, γ'
Flat ΛCDM	*R–L* QSOs	⋯	$0.301^{+0.041}_{-0.069}$	1.660 ± 0.120	0.360 ± 0.120
	L_X–$L_{\rm UV}$ QSOs	⋯	$0.244^{+0.031}_{-0.054}$	25.541 ± 0.090	0.610 ± 0.100

$\overline{E}_{X-\rm UV} = 0.03$ mag, which is comparable in magnitude to the value inferred from the mean for the flat ΛCDM model. The inferred peak values of $E_{X-\rm UV}$ are positive for all the cosmological models. The average value is $\overline{E}_{X-\rm UV} = 0.28 \pm 0.07$ mag, and hence, is larger than the value inferred from the medians. Overall, based on the average median and the peak values, we estimate the X-ray/UV color index of $\overline{E}_{X-\rm UV} \sim 0.03$–$0.28$ mag for our sample.

The positive peak value of the $E_{X-\rm UV}$ distributions for all the cosmological models implies that the extinction is present in the sample, and the effect is stronger in the X-ray band than in the UV band. As we show by the comparison of distributions of δ and $(\log F_{\rm UV} - \log F_X)/[2(1-\gamma')]$ in Appendix B, the positive difference between $\tau_X - \tau_{\rm UV}$ results in the shift of their sum to positive values due to the extinction term. In other words, extinction causes the drop of the X-ray flux to the UV flux density, i.e., $\log F_{\rm UV} - \log F_X$ is positive, which is correlated with the positive difference in optical depths, $\tau_X - \tau_{\rm UV}$. If we assume zero extinction in the UV domain, we can convert $\overline{E}_{X-\rm UV} = 0.03$–$0.28$ mag to the hydrogen column density $N_{\rm H}$ which is customarily used in X-ray studies. Assuming just electron scattering, we derive the mean intrinsic column density of $N_{\rm H} = 4.2 \times 10^{22}$–$3.9 \times 10^{23}\,\mathrm{cm^{-2}}$, which is moderate and in the Compton-thin regime. It can even be lower if the effect is partially due to X-ray absorption. If UV extinction is also present, then the corresponding $N_{\rm H}$ would be higher since we determine only the difference between the two effects. However, it is not likely that the two effects just compensate, so both X-ray and UV extinction effects are noticeable but not dramatically strong in our sample.

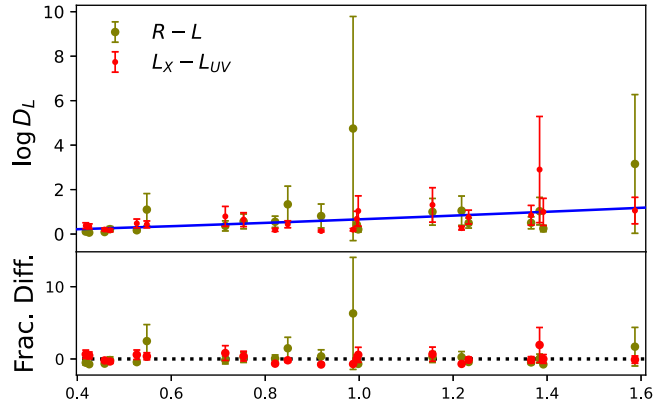

Figure 4. Upper panel: luminosity distances for 21 sources (expressed in 10^4 Mpc) inferred using the *R*–*L* and L_X–$L_{\rm UV}$ relations in the flat ΛCDM model. The blue solid line represents the prediction for the flat ΛCDM model with $\Omega_{m0} = 0.3$. Lower panel: fractional difference between the observed and model-predicted luminosity distances for 21 sources. The colors follow the upper panel convention. The black-dotted line indicates zero fractional difference.

Assuming that in our sample UV extinction is negligible, we can use the mean X-ray extinction determined from our sample to correct the measured values of the $\log D_{L,L_X-L_{\rm UV}}$. All actual values should be larger by 0.032 if corrected for X-ray extinction. When used for the flat ΛCDM cosmology, it systematically pushes the best solution toward significantly higher values of Ω_{m0}, roughly by 0.14, as estimated from the standard cosmology calculator for a median redshift of 0.99, as in our sample. As we show in the derivations in Appendix A, see Equations (A3) and (A7), the extinction affects $\log D_{L,R-L}$ by a factor of $+0.2\tau_{\rm UV}$, while the effect is more pronounced for $\log D_{L,L_X-L_{\rm UV}}$, which is modified by $+0.54\tau_X - 0.33\tau_{\rm UV}$. Hence, for a negligible UV extinction, only the L_X–$L_{\rm UV}$ luminosity distance is affected.

Our analysis result is just the difference between the extinction effect in the X-ray and UV bands and we cannot correct the sample without additional spectral studies.

6. Discussion

We have shown that the $\Delta \log D_L$, and hence, the $E_{X-\rm UV}$ distributions are also significantly asymmetric and their peaks are shifted to the positive side for all the cosmological models considered. We attribute this to the extinction in the X-ray and UV domains with the average value in the range of $\overline{E}_{X-\rm UV} = 0.03$–$0.28$ mag based on the average median and peak values of the $E_{X-\rm UV}$ distributions for all six cosmological models.

This implies that the effect is not very strong but it is present, and it can bias the cosmological results. Our sample of 58 sources contains all sources for which we have luminosity-distance measurements with both methods, and we did not apply any preselection aimed at removing extinction based on spectral studies of individual sources. By calculating the α_{OX} index (Khadka et al. 2023) and considering the *ugriz* magnitudes from the SDSS catalog (see Appendix D), we can conclude that our sample is, for the most part, not heavily obscured and shares properties with the normal (blue) quasar population.

Nevertheless, even though our sample is not heavily obscured, we test the effect of extinction for our sample. By applying X-ray and UV selection cuts, we arrive at a subsample of 21 sources, for which the heavily absorbed sources were removed. Furthermore, we connect $E_{X-\rm UV}$ color index to the more standard E_{B-V} in the optical domain.

6.1. Subsample without Absorbed Sources

To test the extinction effect further, we attempt to remove sources with larger extinction. In our original sample of 58 quasars (Khadka et al. 2023) no preselection was made since the sample of X-ray-detected reverberation-mapped quasars is already limited in size. In the new test, we apply the criteria of Lusso et al. (2020), as described in Khadka et al. (2023), to remove absorbed sources based on available hard X-ray photon indices and far-UV slopes. According to Lusso et al. (2020), the hard X-ray photon index should lie between 1.7 and 2.8, which is satisfied for 41 sources, and the far-UV slope should lie between −0.7 and 1.5, which is satisfied for 27 out of 31 sources for which GALEX EUV magnitudes are available. Combining both criteria yields a subsample of 21 sources, which supposedly does not contain heavily extincted quasars; see Section 2 for the description of the subsample.

For these 21 sources, we construct *R*–*L* and L_X–$L_{\rm UV}$ relations in the flat ΛCDM model ($\Omega_{m0} = 0.3$), see Figure 3, whose parameters are consistent with those for the corresponding relations in the main sample of 58 sources, with a slightly decreased intrinsic scatter of 0.28 and 0.23 dex for the *R*–*L* and L_X–$L_{\rm UV}$ relations, respectively. The removal of absorbed sources is also beneficial for increasing the correlation in both relations. For the *R*–*L* relation, we obtain a Pearson correlation coefficient of $r = 0.63$ ($p = 2.38 \times 10^{-3}$), while for the whole sample of 58 sources, it is $r = 0.56$ ($p = 4.42 \times 10^{-6}$). For the L_X–$L_{\rm UV}$ relation of the subsample of 21 sources, we get $r = 0.86$ ($p = 5.90 \times 10^{-7}$), while for the whole sample, we have $r = 0.78$ ($p = 6.54 \times 10^{-13}$).

We also performed the simultaneous fitting of the L_X–$L_{\rm UV}$ or *R*–*L* relation parameters as well as cosmological parameters for the flat ΛCDM model. For both relations, we list the parameters in Table 4, including their 1σ confidence intervals. The *R*–*L* and L_X−$L_{\rm UV}$ relation parameters for the 21 and 58 sources are consistent within the uncertainties. The differences in γ and β for the *R*–*L* relation are 0.62σ and 0.15σ, respectively. The differences in γ' and β' for the L_X–$L_{\rm UV}$ relation are 0.04σ and 0.88σ, respectively.

Luminosity distances for the 21 sources inferred using the two relations are shown in Figure 4. We show the unnormalized distributions of the luminosity-distance difference in Figure 5 (left panel). We list the basic statistical parameters of the unnormalized distribution in the last line of Table 2. The removal of extincted sources does affect the distribution by decreasing the mean value of the luminosity-distance difference. In addition, skewness becomes negative since the positive tail of the distribution disappears. Fisher's kurtosis also gets smaller because the obscured sources in the tails are removed. On the other hand, the median value increases, which may be the effect of the small size of the subsample. We also fit the $\Delta \log D_{\rm L}$ and $E_{X-\rm UV}$ distributions using the normal Gaussian and the variable Gaussian functions, see the left and the right panels in Figure 5, respectively, with the variable Gaussian fitting the distributions better according to the χ^2 statistic. Actually, the distribution of $E_{X-\rm UV}$ becomes even more asymmetric with $\sigma_+ < \sigma_-$, see Table 3, and the peak is positively shifted with $E_{X-\rm UV} = 0.50 \pm 0.12$ mag, while the median is at ∼0.4 mag. We thus see that the source preselection

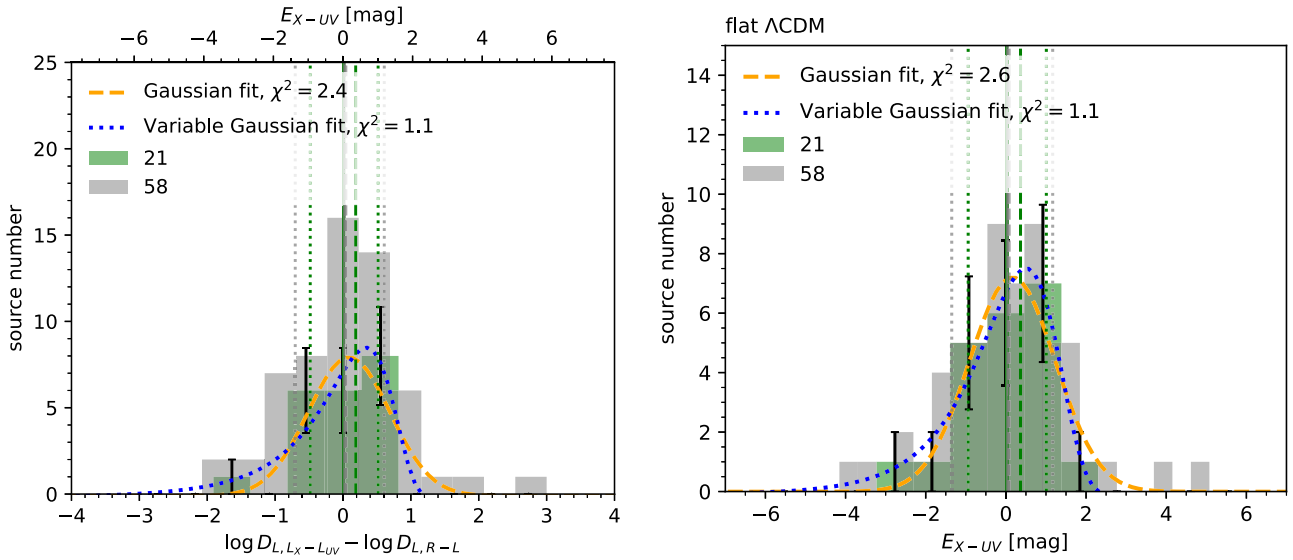

Figure 5. Unnormalized distributions of $\Delta \log D_L = \log D_{L,L_X-L_{UV}} - \log D_{L,R-L}$ and E_{X-UV} for the sample of 21 (58) sources in the flat ΛCDM model in green (gray). Left panel: distribution of the unnormalized luminosity-distance difference $\Delta \log D_L = \log D_{L,L_X-L_{UV}} - \log D_{L,R-L}$ for the subsample of 21 sources. The solid vertical green (gray) line denotes the distribution mean, the green-dashed vertical (gray) line represents the median, and the green-dotted vertical (gray) lines denote the 16th and 84th percentiles. The best-fit Gaussian function is depicted by an orange-dashed line, while the best-fit variable Gaussian function is represented by a blue-dotted line. Right panel: the distribution of E_{X-UV} (in magnitude) in green (gray) for the sample of 21 (58) sources. The vertical lines as well as the blue-dotted and the orange-dashed lines have the same meaning as in the left panel.

alleviates the problem of extinction by removing the outliers and reducing the tails. The change in the distribution characteristics between the samples of 58 and 21 sources indicates that extinction plays a role in increasing the distribution tails consisting of outliers and inducing a positive skewness. However, even after the application of hard X-ray and far-UV cuts, the positive shift of the distribution peak still indicates a contribution from extinction.

The normalized distribution of luminosity-distance differences shown in Figure 6 remains negatively skewed as in the bigger sample of 58 sources analyzed in Khadka et al. (2023). For the sample of 58 sources, the mean of the normalized distribution is negative (−0.116), which indicates that luminosity distances inferred from the L_X–L_{UV} relation are smaller than those inferred from the R–L relation. This is consistent with the overall preference of larger Ω_{m0} for the L_X–L_{UV} relation constructed for 58 sources. The removal of extincted sources and the final subsample of 21 sources exhibit the normalized distribution with a positive mean value (+0.075); hence, this indicates an opposite trend. However, since the subsample of 21 sources is more than a factor of 2 smaller in size, the change in the sign of the mean value may be the result of limited statistics and it does not reflect the trend in the larger samples. However, as for the unnormalized distribution, the absolute value of the mean decreases, which implies that the removal of extincted sources is beneficial for decreasing the luminosity-distance difference between the L_X–L_{UV} and R–L relations.

6.2. Relation to the Extinction Curve and E_{B-V}

Galactic extinction is generally corrected since the $(B-V)$ color excess is known for the whole range of Galactic coordinates (see, e.g., Schlegel et al. 1998). Our sample of 58 sources is in a region in the sky that is far from the Galactic plane, which has a Galactic extinction of $E_{B-V} \sim 0.1$ mag, see Figure 1. However, there still may be uncertainty in the applied

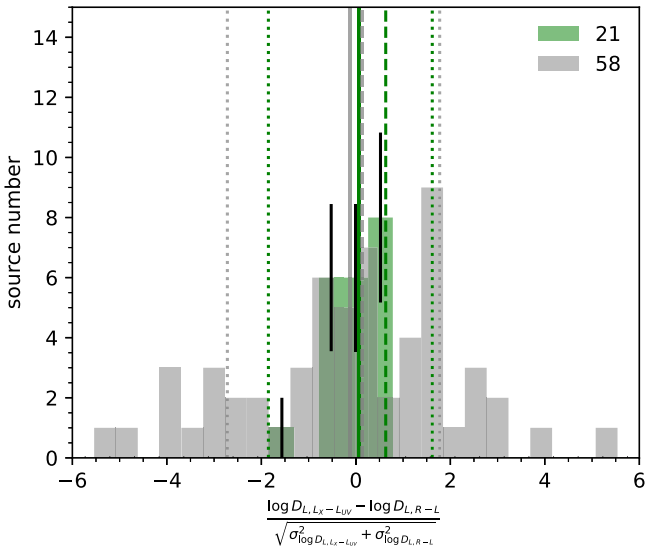

Figure 6. The distribution of $\Delta \log D_L = \log D_{L,L_X-L_{UV}} - \log D_{L,R-L}$ normalized by the square root of the sum of the luminosity-distance uncertainties. The distributions are shown for the whole sample of 58 sources (gray) and the subsample of 21 sources (green). The vertical lines denote the same statistical properties as in Figure 5.

Galactic extinction correction at the level of $E_{B-V} \sim 0.001$ mag. For instance, for NGC 4151 the color index is $E_{B-V} \sim 0.024$ mag according to Schlafly & Finkbeiner (2011), while it was measured to be $E_{B-V} \sim 0.027$ mag according to Schlegel et al. (1998); see the NASA/IPAC Extragalactic Database[15] for the extinction values and their scatter for the other sources.

The more uncertain extinction contribution is due to the QSO optical, UV, and X-ray continuum emissions being affected by intrinsic extinction. For the SDSS data (4576 QSOs), Richards et al. (2003) constructed composite

[15] https://ned.ipac.caltech.edu/

spectra, which they categorized into six composite spectral classes (Composites 1–6). Composite 1 corresponds to sources with intrinsically blue (or optically flat) power-law continua, while Composite 5 corresponds to reddened sources with optically steep power-law continua. Most of the quasars belong to rather bluer composite classes with a color excess of $E_{B-V} < 0.04$ mag, while only ∼10% are reddened.

Based on the composite spectra constructed by Richards et al. (2003), Czerny et al. (2004) derived the extinction curve of QSOs, which is generally similar to the Small Magellanic Cloud extinction curve (Prevot et al. 1984), e.g., lacking the absorption feature at 2200 Å except for the shortest UV wavelengths. The QSO extinction curve can generally be attributed to a circumnuclear dusty shell composed of amorphous carbon grains that lack both silicate and graphite grains based on the corresponding missing spectral features.

In the following, we use the simplified analytical extinction curve in Czerny et al. (2004),

$$\frac{A_\lambda}{E_{B-V}} = -1.36 + 13\log(1/\lambda\ [\mu\mathrm{m}]), \tag{13}$$

and extrapolate it to the UV/X-ray range (2500 Å–2 keV). Here A_λ is an extinction correction at wavelength λ, and E_{B-V} is the color excess measured between the B and V bands, which are customarily used as the extinction measure in the optical/UV band. Subsequently, from the inferred UV/X-ray color excess of $E_{X-\mathrm{UV}} = A_X - A_{\mathrm{UV}} \sim 0.03$–$0.28$ mag (median and peak values, see Table 3), we can use the relation $E_{X-\mathrm{UV}} = 13E_{B-V}\log(\lambda_{\mathrm{UV}}/\lambda_X)$ derived from Equation (13) to obtain the color excess of $E_{B-V} \sim 0.001$–0.01 mag. This can be interpreted to be predominantly the intrinsic color excess expected for the majority of type I QSOs (Richards et al. 2003). This extinction originates in the circumnuclear medium, e.g., in an obscuring torus, a warped disk-like structure, or an outflowing clumpy wind within ∼1 pc from the supermassive black hole (Elvis et al. 2002; Gohil & Ballantyne 2017; Gaskell & Harrington 2018; Gaskell et al. 2023), and the host galaxy interstellar medium, also see Stolc et al. (2023) and Czerny et al. (2023c) for discussions. Dust can also be present on the scales of a few thousand gravitational radii, i.e., on subparsec scales, within the BLR clouds (Pandey et al. 2023). Dusty structures can be located close to a supermassive black hole on subparsec scales, especially for lower-luminosity sources. Considering the source at the low-luminosity end, see Table 1, we have the UV luminosity of $\nu_{\mathrm{UV}}L_{\mathrm{UV}} \sim 1.2 \times 10^{43}\,\mathrm{erg\,s^{-1}}$, which implies the sublimation radius of $r_{\mathrm{sub}} \sim 0.04(T_{\mathrm{sub}}/1500\ \mathrm{K})^{-2.8}(\nu_{\mathrm{UV}}L_{\mathrm{UV}}/10^{43}\mathrm{erg\ s^{-1}})^{1/2}$ pc in the optically thin limit (Barvainis 1987; Zajaček et al. 2014). Actually, in the low-luminosity limit of the Galactic center, compact dusty objects were detected on the scale of ∼1 milliparsec (Gillessen et al. 2012; Peißker et al. 2021), hence understanding the 3D distribution and geometry of dust in galactic nuclei as a function of their accretion rate is relevant for estimating the intrinsic extinction in different wave bands.

Therefore, the discrepancy between luminosity distances inferred using L_X–L_{UV} and R–L relations is expected for any selection of QSOs. This is consistent with the finding that the application of extinction cuts based on the hard X-ray index and the far-UV slope (Lusso et al. 2020) only slightly mitigates the extinction problem, as we showed in Section 6.1, by eliminating the outliers forming the tails. However, other qualitative properties of the $E_{X-\mathrm{UV}}$ distribution, mainly the peak shifted to positive values, persist even after applying the extinction cuts.

We note that including many lower-luminosity QSOs in the sample likely enhances the extinction effect. Weaver & Horne (2022) in their study of 9242 QSOs, all located in SDSS Stripe 82, derived a median extinction E_{B-V} of 0.1 for redshifts around 2 and higher extinction values for lower and higher redshifts (see their Figure A1).

Getting an estimate of the total reddening in AGN is crucial. The typical method involves hydrogen line ratios along UV, optical, and near-infrared wavelengths such as Lyα/Hβ, Hα/Hβ, and Paβ/Hβ (Osterbrock & Ferland 2006; Panda 2022; Gaskell et al. 2023). Other methods require simultaneous measurements in a broad wavelength range (Shuder & MacAlpine 1979; Choloniewski 1981; Cackett et al. 2007). Unfortunately, none of these methods can be implemented for our sample due to the lack of broadband measurements.

7. Conclusions

We find that the extinction (scattering and absorption) of X-ray and UV photons from QSOs contributes to the discrepancy between luminosity distances inferred using L_X–L_{UV} and R–L relations.

For the nonzero luminosity-distance difference, i.e., $\Delta\log D_L = \log D_{L,L_X-L_{\mathrm{UV}}} - \log D_{L,R-L}$, the extinction term is equal to $(\Delta\log D_L)_{\mathrm{ext}} = (\tau_X - \tau_{\mathrm{UV}})\log e/[2(1-\gamma')]$, where τ_X and τ_{UV} are optical depths in the X-ray and UV domains, respectively, and γ' is the slope of the L_X–L_{UV} relation. We found that the distributions of $\Delta\log D_{\mathrm{L}}$ are asymmetric and positively shifted for all the six cosmological models considered. We estimated an average X-ray/UV color index of $\overline{E}_{X-\mathrm{UV}} = 0.03$–$0.28$ mag in our sample, based on all six distribution median and peak values. We have shown that this amount of extinction is mild and overall typical for the majority of type I QSOs since it is supposed to originate in the circumnuclear and interstellar media of host galaxies (Czerny et al. 2004). The dust-related systematic problem does not seem to be completely removed by standard hard X-ray and far-UV extinction cuts; hence, some caution is necessary when interpreting the results (Khadka & Ratra 2021, 2022). Therefore, using at least two complementary methods for larger samples in the future is recommended.

Acknowledgments

This research was supported in part by Dr. Richard Jelsma (a Bellarmine University donor), Research Foundation for the SUNY, US DOE grant DE-SC0011840, by the Polish Funding Agency National Science Center, project 2017/26/A/ST9/00756 (Maestro 9), by GAČR EXPRO grant 21-13491X, by Millenium Nucleus NCN19$_{058}$ (TITANs), and by the Conselho Nacional de Desenvolvimento Científico e Tecnológico (CNPq) Fellowships (164753/2020-6 and 313497/2022-2). B.C. and M. Z. acknowledge the Czech-Polish mobility program (MŠMT 8J20PL037 and PPN/BCZ/2019/1/00069). This project has received funding from the European Research Council (ERC) under the European Union's Horizon 2020 research and innovation program (grant agreement No. [951549]). Part of

the computation for this project was performed on the Beocat Research Cluster at Kansas State University.

Appendix A
Derivation of $D_{L,R-L}$, $D_{L,L_X-L_{\rm UV}}$, and $E_{X-{\rm UV}}$ Expressions in the Presence of Extinction

A.1. Derivation of $\mathrm{D_{L,R-L}}$

Using the *R–L* relation in the form of

$$\log\left(\frac{\tau}{\rm days}\right)=\beta+\gamma\log\left(\frac{L_{3000}}{10^{\eta}\ {\rm erg\ s^{-1}}}\right), \tag{A1}$$

where the monochromatic luminosity L_{3000} can be expressed in the form of the UV flux density at 2500 Å as $L_{3000,\rm int}=4\pi D_L^2 F_{3000,\nu}\nu_{3000}=4\pi D_L^2 F_{\rm UV}(2500/3000)^{\alpha_\nu}\nu_{3000}$, the *R–L*-based luminosity distance can be evaluated as

$$\log D_{L,R-L}=\frac{1}{2\gamma}(\log\tau-\beta)-\frac{1}{2}[\log(4\pi)-\eta+15.036]-\frac{1}{2}\log F_{\rm UV}, \tag{A2}$$

where we used $\alpha_\nu\sim-0.45$ for the mean QSO continuum slope (Vanden Berk et al. 2020). To extract the extinction term that modifies $\log D_{L,R-L}$, we use the extinction law in the form of $F_{\rm UV}=F_{\rm UV,\ int}e^{-\tau_{\rm UV}}$, where $F_{\rm UV,\ int}$ is the intrinsic QSO UV flux density. Equation (A2) can then be rewritten as

$$\log D_{L,R-L}=\frac{1}{2\gamma}(\log\tau-\beta)-\frac{1}{2}[\log(4\pi)-\eta+15.036]-\frac{1}{2}\log F_{\rm UV,\ int}+\frac{\log e}{2}\tau_{\rm UV}, \tag{A3}$$

where the nonzero UV optical depth clearly increases the *R–L* luminosity distance with the term $+\frac{\log e}{2}\tau_{\rm UV}\sim+0.2\tau_{\rm UV}$.

A.2. Derivation of $D_{L,L_X-L_{\rm UV}}$

Analogously, from the L_X–$L_{\rm UV}$ power-law relation parameterized as

$$\log\left(\frac{L_X}{\rm erg\ s^{-1}\,Hz^{-1}}\right)=\beta'+\gamma'\log\left(\frac{L_{\rm UV}}{10^{\eta'}\ {\rm erg\ s^{-1}Hz^{-1}}}\right), \tag{A4}$$

we can derive the L_X–$L_{\rm UV}$-based luminosity distance $D_{L,L_X-L_{\rm UV}}$ that depends on X-ray and UV monochromatic flux densities at 2 keV and 2500 Å F_X and $F_{\rm UV}$, respectively. The relation is as follows:

$$\log D_{L,L_X-L_{\rm UV}}=\frac{\beta'-\gamma'\eta'}{2(1-\gamma')}-\frac{\log(4\pi)}{2}+\frac{\gamma'\log F_{\rm UV}}{2(1-\gamma')}-\frac{\log F_X}{2(1-\gamma')}. \tag{A5}$$

Using the extinction laws in the UV and the X-ray domains, $F_{\rm UV}=F_{\rm UV,\ int}e^{-\tau_{\rm UV}}$ and $F_X=F_{\rm X,int}e^{-\tau_X}$, respectively, we can express Equation (A5) as

$$\log D_{L,L_X-L_{\rm UV}}=\frac{\beta'-\gamma'\eta'}{2(1-\gamma')}-\frac{\log(4\pi)}{2}+\frac{\gamma'(\log F_{\rm UV,\ int}-\tau_{\rm UV}\log e)}{2(1-\gamma')}-\frac{\log F_{\rm X,int}-\tau_X\log e}{2(1-\gamma')}. \tag{A6}$$

By separating intrinsic flux density terms from the extinction terms, we obtain

$$\log D_{L,L_X-L_{\rm UV}}=\frac{\beta'-\gamma'\eta'}{2(1-\gamma')}-\frac{\log(4\pi)}{2}+\frac{\gamma'\log F_{\rm UV,\ int}-\log F_{\rm X,int}}{2(1-\gamma')}+\frac{\tau_X\log e}{2(1-\gamma')}-\frac{\tau_{\rm UV}\gamma'\log e}{2(1-\gamma')}. \tag{A7}$$

Hence, for $\gamma'\sim0.6$ the extinction modifies $\log D_{L,L_X-L_{\rm UV}}$ by $\sim+0.54\tau_X-0.33\tau_{\rm UV}$, i.e., the L_X–$L_{\rm UV}$-based luminosity distance depends more strongly on the UV optical depth (it is decreased) than the *R–L*-based luminosity distance. In addition, it is increased by the nonzero X-ray optical depth, which is not present in the *R–L*-based luminosity-distance relation. Also, it is essential to note that the extinction effect for the L_X–$L_{\rm UV}$ relation depends on its slope γ'; hence, this leads to a circularity problem in evaluating the extinction terms.

A.3. Derivation of $\mathrm{E_{X-UV}}$

The color index between the X-ray and UV domains is defined as $E_{X-{\rm UV}}\equiv_{AX}-A_{\rm UV}=1.086(\tau_X-\tau_{\rm UV})$. To obtain $E_{X-{\rm UV}}$, we first calculate the difference between $\Delta\log D_{\rm L}=\log D_{L,L_X-L_{\rm UV}}-\log D_{L,R-L}=\log(D_{L,L_X-L_{\rm UV}}/D_{L,R-L})$ using Equations (A7) and (A3),

$$\Delta\log D_L=\overbrace{\underbrace{\frac{\beta'-\gamma'\eta'}{2(1-\gamma')}+\frac{\beta-\log\tau}{2\gamma}-\frac{\eta}{2}+7.518+\frac{\log F_{\rm UV,\ int}-\log F_{\rm X,ir}}{2(1-\gamma')}}_{=0\text{ for intrinsic quasar emission}}}^{\delta}+\underbrace{\frac{(\tau_X-\tau_{\rm UV})\log e}{2(1-\gamma')}}_{\text{extinction contribution}}, \tag{A8}$$

where the term $\delta+(\log F_{\rm UV,\ int}-\log F_{\rm X,int})/[2(1-\gamma')]$ is assumed to sum to zero for the intrinsic quasar emission, and hence the luminosity-distance difference for any source is zero without extinction. The nonzero difference is thus related to the extinction term, from which the difference in the optical depth is $\tau_X-\tau_{\rm UV}=2(1-\gamma')\Delta\log D_L/\log e$.

Finally, the color index $E_{X-{\rm UV}}$ can be expressed just as a function of the luminosity-distance difference and the slope

γ' of the L_X–$L_{\rm UV}$ relation

$$E_{X-{\rm UV}} = (2.172/\log e)(1-\gamma')\Delta\log D_L \simeq 5.001(1-\gamma')\Delta\log D_L. \quad \text{(A9)}$$

Appendix B
δ versus $(\log F_{\rm UV} - \log F_X)/[2(1-\gamma')]$ Distributions

To illustrate Equation (A8), i.e., $\Delta\log D_L = \delta + (\log F_{\rm UV} - \log F_X)/[2(1-\gamma')]$, we compare distributions of δ, $(\log F_{\rm UV} - \log F_X)/[2(1-\gamma')]$, and their sum $\Delta\log D_L$ in Figure 7 for 58 sources and flat and non-flat ΛCDM models (distributions are similar for the other cosmological models). The mean value of δ is always negative, while the mean value of $(\log F_{\rm UV} - \log F_X)/[2(1-\gamma')]$ is positive and of a comparable magnitude. However, their sum, which is equivalent to the difference in luminosity-distance logarithms, is characterized by a distribution with positive skewness and a nonzero mean in all cases (see Figure 7 and Table 2 for the details). This behavior can qualitatively be attributed to the extinction term in Equation (A8) proportional to $\tau_X - \tau_{\rm UV}$, from which the color index $E_{X-{\rm UV}}$ can be quantified using Equation (A9). If $\tau_X > \tau_{\rm UV}$, then the extinction term is positive and the distribution of $\Delta\log D_L$ is shifted to positive values. The positive skewness is mainly given by the fact that for larger $\log F_{\rm UV} - \log F_X$ the optical depth difference tends to be greater since $\tau_X > \tau_{\rm UV}$ for sources with a more absorbed X-ray emission.

For the sample of 21 sources that pass the reddening criteria of Lusso et al. (2020), the mean value of $\Delta\log D_L = \delta + (\log F_{\rm UV} - \log F_X)/[2(1-\gamma')]$ decreases for the flat ΛCDM model in comparison with the full sample of 58 sources (0.011 versus 0.017), see Figure 8. This implies that the reddening cuts are beneficial for decreasing the offset; however, the intrinsic extinction contribution seems to still be present.

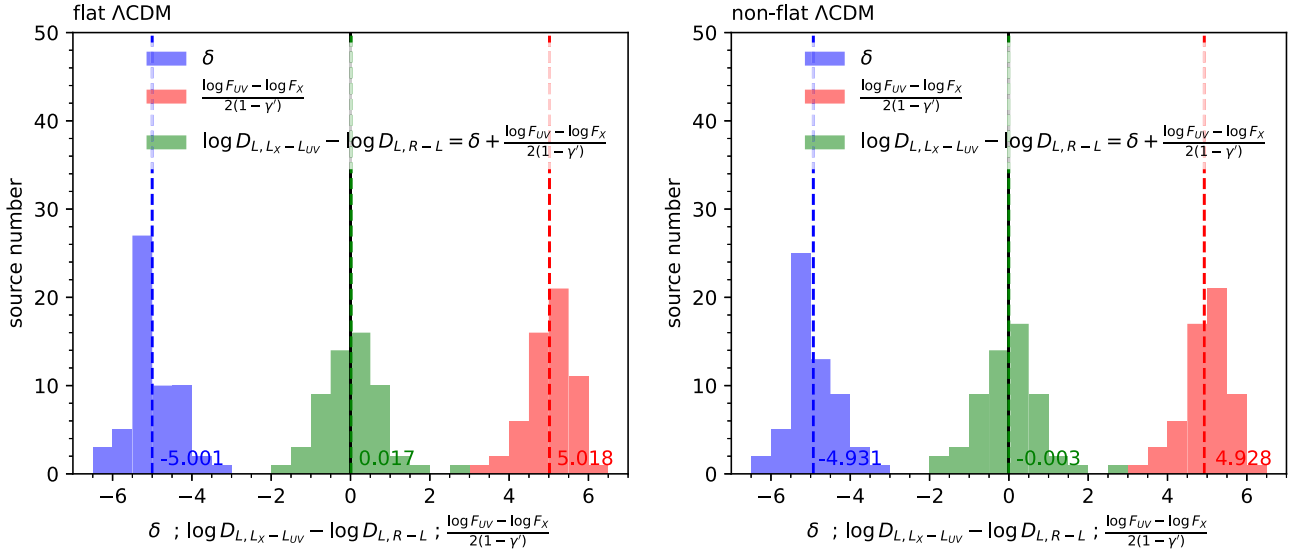

Figure 7. Comparison of distributions of the factor δ (blue histogram; see Equation (A8)), the factor $(\log F_{\rm UV} - \log F_X)/[2(1-\gamma')]$ (red histogram), and $\log D_{L,L_X-L_{\rm UV}} - \log D_{L,R-L} = \delta + (\log F_{\rm UV} - \log F_X)/[2(1-\gamma')]$ (green histogram) for 58 sources for the flat and non-flat ΛCDM cosmological models in the left and the right panels, respectively. The black solid vertical line denotes zero, while the colored dashed vertical lines (blue, green, and red) represent the means of the corresponding distributions.

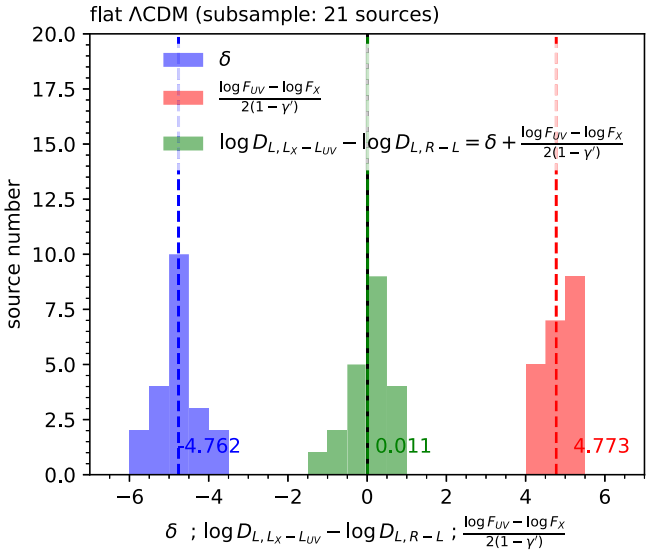

Figure 8. Comparison of distributions of the factor δ (blue histogram; see Equation (A8)), the factor $(\log F_{\rm UV} - \log F_X)/[2(1-\gamma')]$ (red histogram), and $\log D_{L,L_X-L_{\rm UV}} - \log D_{L,R-L} = \delta + (\log F_{\rm UV} - \log F_X)/[2(1-\gamma')]$ (green histogram) for the subsample of 21 sources for the flat ΛCDM cosmological model. The black solid vertical line denotes zero, while the colored dashed vertical lines (blue, green, and red) represent the means of the corresponding distributions.

Appendix C
$E_{X-\rm UV}$ Distributions

Using Equation (12), i.e., $E_{X-\rm UV} \equiv A_X - A_{\rm UV} \simeq 5.001(1-\gamma')\langle(\Delta \log D_{\rm L})_{\rm ext}\rangle$, we construct distributions of the color index $E_{X-\rm UV}$ from the luminosity-distance differences for each source. We show histograms of $E_{X-\rm UV}$ for six cosmological models (flat and non-flat ΛCDM, XCDM, and ϕCDM models from the top to the bottom rows) in Figure 9. All of the 58 sources have $E_{X-\rm UV}$ in the interval (−6,6) and the histogram bin widths are determined based on Knuth's rule. The red solid vertical line represents the distribution mean, the dashed vertical line denotes the median, and the red-dotted lines represent the 16th and 84th percentiles. We also perform fits of Gaussian and variable Gaussian functions to all the distributions, which are shown by orange-dashed and blue-dotted lines, respectively.

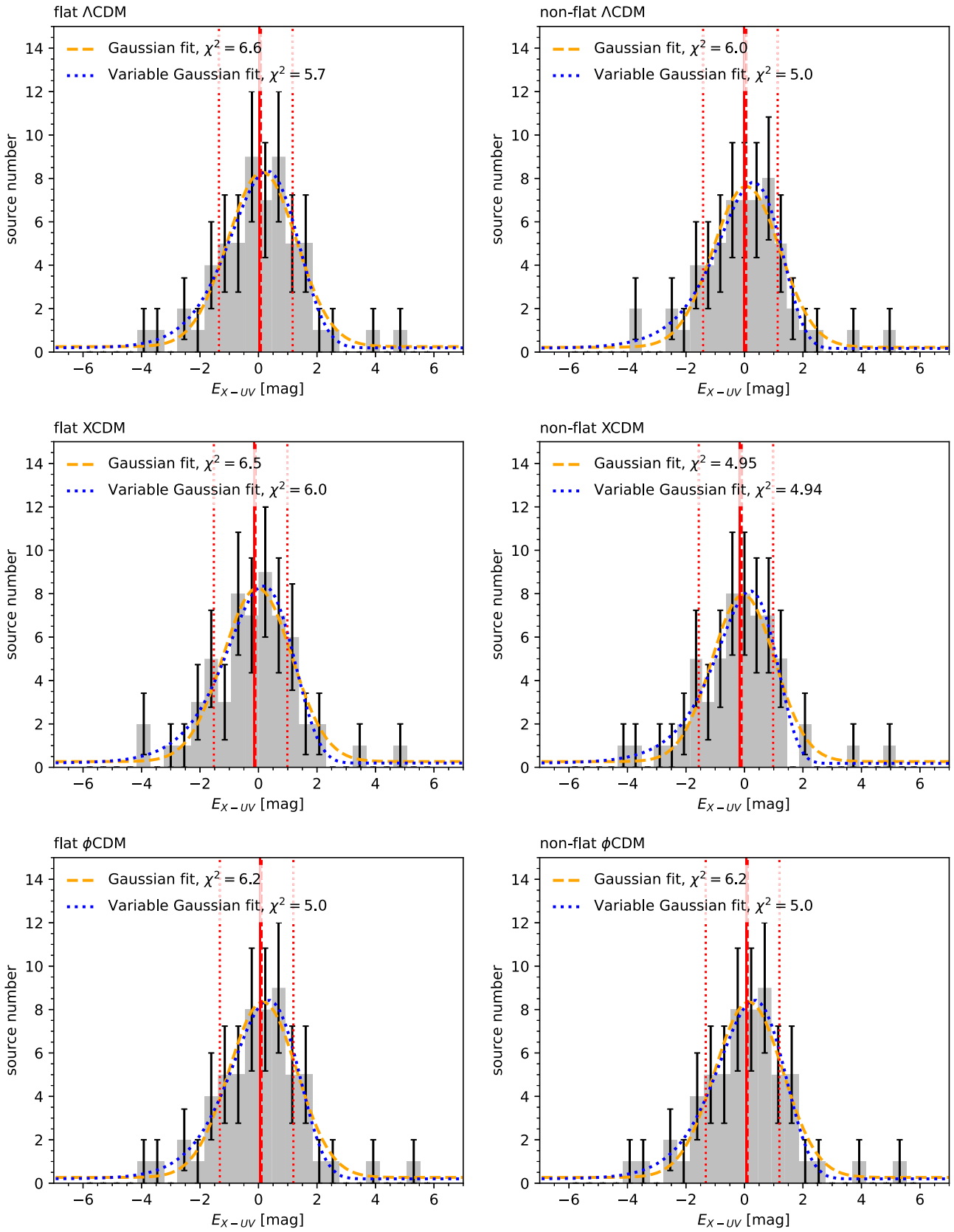

Figure 9. Distributions of the X-ray/UV color indices $E_{X-\mathrm{UV}}$ for 58 sources for the flat and non-flat ΛCDM, XCDM, and ϕCDM cosmological models (from top to bottom row). The X-ray/UV color index $E_{X-\mathrm{UV}} = 5.001(1-\gamma')\Delta \log D_{\mathrm{L}}$ is calculated based on the luminosity distances for each source and the L_X–L_{UV} relation slope for each cosmological model. Solid red vertical lines represent $E_{X-\mathrm{UV}}$ means, red-dashed vertical lines represent $E_{X-\mathrm{UV}}$ medians, and red-dotted vertical lines represent the corresponding 16th and 84th percentiles. The bin width is set based on the Knuth binning algorithm and the histogram y uncertainties for each bin are $\sigma_{y,i} = \sqrt{N_i}$, where N_i is the number of points in each bin. The best-fit Gaussian function is represented by an orange-dashed line, while the best-fit variable Gaussian function is depicted by a blue-dotted line.

Appendix D
Inference of the Reddening Using the SDSS Magnitudes

An alternative possibility to infer the reddening effect in our sample involves using the *ugriz* magnitudes from the SDSS database. To compare the behavior of our sample, we have adopted the blue and red quasar samples defined by Glikman et al. (2022). They considered red quasars as sources that have $E_{B-V} > 0.25$. We have obtained the u and z magnitudes from the SDSS database, which are not reported by Glikman et al. (2022). The SDSS magnitudes for the Mg II reverberation-mapped sample were taken from Shen et al. (2019). In all cases, the magnitudes were corrected for galactic extinction. Color–color plots are shown in Figure 10, where it is possible to observe the difference between the blue and the red samples. Most of the Mg II reverberation-mapped sources are located at the left, bluer part of the distribution, which indicates that they have $E_{B-V} < 0.25$. This result is consistent with the one found in Section 5. In Figure 10 we also identify the 21 sources that satisfy the selection criteria of Lusso et al. (2020), see Section 2; these exhibit the same behavior as the full 58 source sample. Some of our sources are located in the red quasar zone or show peculiar behavior to the rest of the sample. We have identified three sources (SDSS J141110.95 +524815.5, SDSS J142041.78+521701.6, and SDSSJ141645.58 +534446.8) that are in the red zone or show different behavior in at least two color–color diagrams. The consistent location of SDSS J141110.95+524815.5 and SDSS J142041.78+521701.6 in the red quasar zone suggests that they have a high extinction. SDSS J141645.58+534446.8 shows extreme behavior, but it is not necessarily located in the red quasar region. However, a visual inspection of the spectrum shows a flat continuum in the optical range, which suggests a high degree of reddening. One of these sources (SDSS J142041.78+521701.6) belongs to the 21 source sample. Thus, the criteria based on the hard X-ray index and far-UV slope criteria of Lusso et al. (2010) seem to be effective in cleaning the sample.

Figure 11 shows the $u-g$ and $g-i$ distributions as a function of redshift. Using the Calzetti et al. (2000) extinction law, we obtained the expected change in relative color as a function of redshift for $E_{B-V} = 0.04$, 0.09, 0.15, and 0.2. We assumed a continuum slope of $\alpha = -1.56$ and $\alpha = -0.45$ following the composite spectrum of Vanden Berk et al. (2001) for $u-g$ and $g-i$ colors, respectively. The behavior is the same as the one in Figure 10, red and blue quasar samples occupy different zones in the diagrams, and most of the Mg II reverberation-mapped sources overlap with the blue quasar sample. The E_{B-V} curves indicate that our sample has $E_{B-V} < 0.2$. $E_{B-V} = 0.09$ is in the middle of the distribution, which supports the results found in Section 5. In Figure 11 we also show the limit for red sources at $u-g = 0.8$ according to Richards et al. (2003), which coincides with the $E_{B-V} = 0.2$ curve. Since most of the reverberation-mapped sample is to the left of this curve, this suggests that our sample is more consistent with a blue behavior. The E_{B-V} curves confirm the red color of the three sources identified above. These objects should be excluded from future analyses.

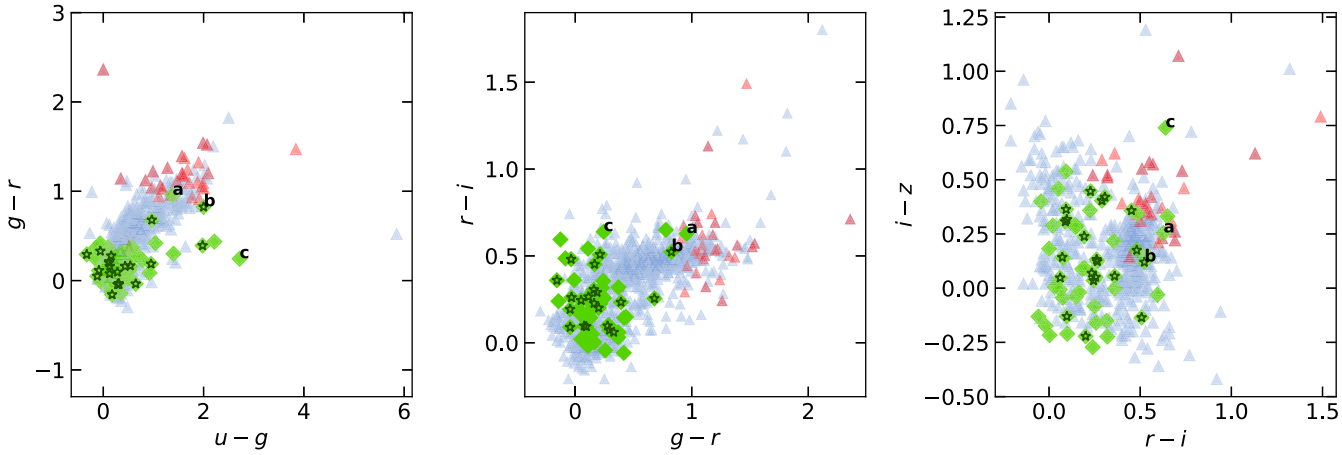

Figure 10. Color–color diagrams for blue and red quasar (triangle symbols) samples defined by Glikman et al. (2022), and the Mg II reverberation-mapped sample (green diamond symbols). Star symbols correspond to the 21 objects described in Section 2. Lowercase letters identify the redder objects of the Mg II reverberation-mapped sample: (a) SDSS J141110.95+524815.5 , (b) SDSS J142041.78+521701.6 , (c) SDSS J141645.58+534446.8.

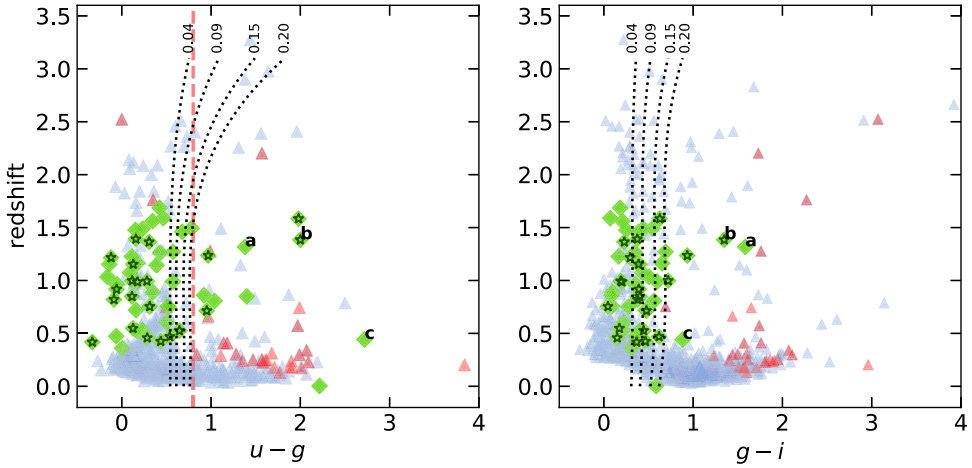

Figure 11. Redshift-color diagrams. The dotted lines represent the expected change in relative color as a function of redshift for $E_{B-V} = 0.04$, 0.09, 0.15, and 0.20 from left to right, respectively. To estimate the change in E_{B-V} as a function of redshift, we used the Calzetti et al. (2000) extinction law. In the left panel, the vertical red-dashed line indicates the limit for red quasars according to Richards et al. (2003) at $u - g = 0.8$. Symbols have the same meaning as in Figure 10.

ORCID iDs

Michal Zajaček https://orcid.org/0000-0001-6450-1187
Bożena Czerny https://orcid.org/0000-0001-5848-4333
Narayan Khadka https://orcid.org/0000-0001-5512-2716
Mary Loli Martínez-Aldama https://orcid.org/0000-0002-7843-7689
Raj Prince https://orcid.org/0000-0002-1173-7310
Swayamtrupta Panda https://orcid.org/0000-0002-5854-7426
Bharat Ratra https://orcid.org/0000-0002-7307-0726

References

Abdalla, E., Abellán, G. F., Aboubrahim, A., et al. 2022, JHEAp, 34, 49
Adil, A., Albrecht, A., & Knox, L. 2023, PhRvD, 107, 063521
Almeida, A., Anderson, S. F., Argudo-Fernández, M., et al. 2023, ApJS, 267, 44
Banerjee, A., Colgáin, Ó., Sasaki, E., Sheikh-Jabbari, M., & Yang, T, M. M. 2021, PhLB, 818, 136366
Barlow, R. 2004, arXiv:physics/0406120
Barvainis, R. 1987, ApJ, 320, 537
Birrer, S., Shajib, A. J., Galan, A., et al. 2020, A&A, 643, A165
Brout, D., Scolnic, D., Popovic, B., et al. 2022, ApJ, 938, 110
Brum, C., Diniz, M. R., Riffel, R. A., et al. 2019, MNRAS, 486, 691
Cackett, E. M., Horne, K., & Winkler, H. 2007, MNRAS, 380, 669
Calzetti, D., Armus, L., Bohlin, R. C., et al. 2000, ApJ, 533, 682
Cao, S., Khadka, N., & Ratra, B. 2022a, MNRAS, 510, 2928
Cao, S., & Ratra, B. 2022, MNRAS, 513, 5686
Cao, S., & Ratra, B. 2023a, PhRvD, 107, 103521
Cao, S., & Ratra, B. 2023b, arXiv:2310.15812
Cao, S., Ryan, J., Khadka, N., & Ratra, B. 2021a, MNRAS, 501, 1520
Cao, S., Ryan, J., & Ratra, B. 2020, MNRAS, 497, 3191
Cao, S., Ryan, J., & Ratra, B. 2021b, MNRAS, 504, 300
Cao, S., Ryan, J., & Ratra, B. 2022b, MNRAS, 509, 4745
Cao, S., Zajaček, M., Czerny, B., Panda, S., & Ratra, B. 2023, arXiv:2309.16516
Cao, S., Zajaček, M., Panda, S., et al. 2022c, MNRAS, 516, 1721
Cao, S., Zheng, X., Biesiada, M., et al. 2017, A&A, 606, A15
Choloniewski, J. 1981, AcA, 31, 293
Collier, S., Horne, K., Wanders, I., & Peterson, B. M. 1999, MNRAS Lett., 302, L24
Czerny, B., Cao, S., Jaiswal, V. K., et al. 2023a, Ap&SS, 368, 8
Czerny, B., Li, J., Loska, Z., & Szczerba, R. 2004, MNRAS Lett., 348, L54
Czerny, B., Martínez-Aldama, M. L., Wojtkowska, G., et al. 2021, AcPPA, 139, 389
Czerny, B., Panda, S., Prince, R., et al. 2023b, A&A, 675, A163
Czerny, B., Zajaček, M., Naddaf, M.-H., et al. 2023c, EPJD, 77, 56
Dahiya, D., & Jain, D. 2023, RAA, 23, 095001
Dainotti, M. G., Bargiacchi, G., Lenart, A. Ł., et al. 2022, ApJ, 931, 106
de Cruz Pérez, J., Park, C.-G., & Ratra, B. 2023, PhRvD, 107, 063522
de Cruz Perez, J., Sola Peracaula, J., Gomez-Valent, A., & Moreno-Pulido, C. 2021, arXiv:2110.07569
DES Collaboration, Abdalla, F. B., Avila, S., et al. 2019, PhRvD, 99, 123505
Dhawan, S., Alsing, J., & Vagnozzi, S. 2021, MNRAS Lett., 506, L1
Di Valentino, E., Melchiorri, A., & Silk, J. 2021, ApJL, 908, L9
Dong, F., Park, C., Hong, S. E., et al. 2023, ApJ, 953, 98
eBOSS Collaboration, Alam, S., Aubert, M., et al. 2021, PhRvD, 103, 083533
Eckart, A., Hüttemann, A., Kiefer, C., et al. 2017, FoPh, 47, 553
Efstathiou, G., & Gratton, S. 2020, MNRAS Lett., 496, L91
Elvis, M., & Karovska, M. 2002, ApJL, 581, L67
Elvis, M., Marengo, M., & Karovska, M. 2002, ApJL, 567, L107
Favale, A., Gómez-Valent, A., & Migliaccio, M. 2023, MNRAS, 523, 3406
Gaskell, C. M., Anderson, F. C., Birmingham, S. Á., & Ghosh, S. 2023, MNRAS, 519, 4082
Gaskell, C. M., & Harrington, P. Z. 2018, MNRAS, 478, 1660
Geng, C.-Q., Hsu, Y.-T., & Lu, J.-R. 2022, ApJ, 926, 74
Gillessen, S., Genzel, R., Fritz, T. K., et al. 2012, Natur, 481, 51
Glanville, A., Howlett, C., & Davis, T. 2022, MNRAS, 517, 3087
Glikman, E., Lacy, M., LaMassa, S., et al. 2022, ApJ, 934, 119
Gohil, R., & Ballantyne, D. R. 2017, MNRAS, 468, 4944
Homayouni, Y., Trump, J. R., Grier, C. J., et al. 2020, ApJ, 901, 55
Hu, J. P., & Wang, F. Y. 2022, A&A, 661, A71
Hu, J.-P., & Wang, F.-Y. 2023, Univ, 9, 94
Jesus, J. F., Valentim, R., Escobal, A. A., Pereira, S. H., & Benndorf, D. 2022, JCAP, 2022, 037
Ivezić, Ž., Kahn, S. M., Tyson, J. A., et al. 2019, ApJ, 873, 111
Karas, V., Svoboda, J., & Zajaček, M. 2021, in RAGtime: Workshops on black holes and neutron stars, 154
Khadka, N., Luongo, O., Muccino, M., & Ratra, B. 2021a, JCAP, 2021, 042
Khadka, N., Martínez-Aldama, M. L., Zajaček, M., Czerny, B., & Ratra, B. 2022a, MNRAS, 513, 1985
Khadka, N., & Ratra, B. 2020a, MNRAS, 492, 4456
Khadka, N., & Ratra, B. 2020b, MNRAS, 497, 263
Khadka, N., & Ratra, B. 2020c, MNRAS, 499, 391
Khadka, N., & Ratra, B. 2021, MNRAS, 502, 6140
Khadka, N., & Ratra, B. 2022, MNRAS, 510, 2753
Khadka, N., Yu, Z., Zajaček, M., et al. 2021b, MNRAS, 508, 4722
Khadka, N., Zajaček, M., Panda, S., Martínez-Aldama, M. L., & Ratra, B. 2022b, MNRAS, 515, 3729
Khadka, N., Zajaček, M., Prince, R., et al. 2023, MNRAS, 522, 1247
Knuth, K. H. 2006, arXiv:physics/0605197
Li, X., Keeley, R. E., Shafieloo, A., et al. 2021, MNRAS, 507, 919
Lian, Y., Cao, S., Biesiada, M., et al. 2021, MNRAS, 505, 2111
Lusso, E., Comastri, A., Vignali, C., et al. 2010, A&A, 512, A34
Lusso, E., Risaliti, G., Nardini, E., et al. 2020, A&A, 642, A150
Martínez-Aldama, M. L., Czerny, B., Kawka, D., et al. 2019, ApJ, 883, 170
Metzroth, K. G., Onken, C. A., & Peterson, B. M. 2006, ApJ, 647, 901
Moresco, M., Amati, L., Amendola, L., et al. 2022, LRR, 25, 6
Mukherjee, P., & Banerjee, N. 2022, PhRvD, 105, 063516
Ooba, J., Ratra, B., & Sugiyama, N. 2018a, ApJ, 869, 34

Ooba, J., Ratra, B., & Sugiyama, N. 2018b, ApJ, 866, 68
Ooba, J., Ratra, B., & Sugiyama, N. 2019, Ap&SS, 364, 176
Osterbrock, D. E., & Ferland, G. J. 2006, Astrophysics of gaseous nebulae and active galactic nuclei (Sausalito, CA: Univ. Science Books)
Panda, S. 2022, FrASS, 9, 850409
Panda, S., Martínez-Aldama, M. L., & Zajaček, M. 2019a, FrASS, 6, 75
Panda, S., & Marziani, P. 2023, FrASS, 10, 31
Panda, S., Marziani, P., & Czerny, B. 2019b, ApJ, 882, 79
Panda, S., & Śniegowska, M. 2022, arXiv:2206.10056
Pandey, A., Czerny, B., Panda, S., et al. 2023, A&A, 680, A102
Park, C.-G., & Ratra, B. 2018, ApJ, 868, 83
Park, C.-G., & Ratra, B. 2019a, Ap&SS, 364, 82
Park, C.-G., & Ratra, B. 2019b, Ap&SS, 364, 134
Park, C.-G., & Ratra, B. 2020, PhRvD, 101, 083508
Pavlov, A., Westmoreland, S., Saaidi, K., & Ratra, B. 2013, PhRvD, 88, 123513
Peebles, P. J. E. 1984, ApJ, 284, 439
Peebles, P. J. E., & Ratra, B. 1988, ApJL, 325, L17
Peißker, F., Zajaček, M., Eckart, A., et al. 2021, ApJ, 923, 69
Perivolaropoulos, L., & Skara, F. 2022, NewAR, 95, 101659
Petrosian, V., Singal, J., & Mutchnick, S. 2022, ApJL, 935, L19
Planck Collaboration 2020, A&A, 641, A6
Prevot, M. L., Lequeux, J., Maurice, E., Prevot, L., & Rocca-Volmerange, B. 1984, A&A, 132, 389
Rana, A., Jain, D., Mahajan, S., & Mukherjee, A. 2017, JCAP, 2017, 028
Ratra, B., & Peebles, P. J. E. 1988, PhRvD, 37, 3406
Renzi, F., Hogg, N. B., & Giarè, W. 2022, MNRAS, 513, 4004
Rezaei, M., Solà Peracaula, J., & Malekjani, M. 2022, MNRAS, 509, 2593
Richards, G. T., Hall, P. B., Vanden Berk, D. E., et al. 2003, AJ, 126, 1131
Risaliti, G., & Lusso, E. 2015, ApJ, 815, 33
Risaliti, G., & Lusso, E. 2019, NatAs, 3, 272
Ryan, J., Chen, Y., & Ratra, B. 2019, MNRAS, 488, 3844
Schlafly, E. F., & Finkbeiner, D. P. 2011, ApJ, 737, 103
Schlegel, D. J., Finkbeiner, D. P., & Davis, M. 1998, ApJ, 500, 525
Colgáin, E. Ó., Sheikh-Jabbari, M. M., Solomon, R., et al. 2022, PhRvD, 106, L041301
Shen, Y., Hall, P. B., Horne, K., et al. 2019, ApJS, 241, 34
Shen, Y., Horne, K., Grier, C. J., et al. 2016, ApJ, 818, 30
Shuder, J. M., & MacAlpine, G. M. 1979, ApJ, 230, 348
Singh, A., Sangwan, A., & Jassal, H. K. 2019, JCAP, 2019, 047
Sinha, S., & Banerjee, N. 2021, JCAP, 2021, 060
Solà Peracaula, J., Gómez-Valent, A., & de Cruz Pérez, J. 2019, PDU, 25, 100311
Stevens, J., Khoraminezhad, H., & Saito, S. 2023, JCAP, 2023, 046
Stolc, M., Zajaček, M., Czerny, B., & Karas, V. 2023, MNRAS, 522, 2869
Ureña-López, L. A., & Roy, N. 2020, PhRvD, 102, 063510
Vagnozzi, S., Di Valentino, E., Gariazzo, S., et al. 2021a, PDU, 33, 100851
Vagnozzi, S., Loeb, A., & Moresco, M. 2021b, ApJ, 908, 84
Van Raamsdonk, M., & Waddell, C. 2023, arXiv:2305.04946
Vanden Berk, D. E., Richards, G. T., Bauer, A., et al. 2001, AJ, 122, 549
Vanden Berk, D. E., Wesolowski, S. C., Yeckley, M. J., et al. 2020, MNRAS, 493, 2745
Wang, F., Yang, J., Fan, X., et al. 2021, ApJL, 907, L1
Wang, J.-M., Songsheng, Y.-Y., Li, Y.-R., Du, P., & Zhang, Z.-X. 2020, NatAs, 4, 517
Weaver, J. R., & Horne, K. 2022, MNRAS, 512, 899
Wu, P.-J., Qi, J.-Z., & Zhang, X. 2023, ChPhC, 47, 055106
Xu, T., Chen, Y., Xu, L., & Cao, S. 2022, PDU, 36, 101023
Yu, H., Ratra, B., & Wang, F.-Y. 2018, ApJ, 856, 3
Yu, Z., Martini, P., Penton, A., et al. 2021, MNRAS, 507, 3771
Zajaček, M., Czerny, B., Jaiswal, V. K., et al. 2023, arXiv:2306.15082
Zajaček, M., Czerny, B., Martinez-Aldama, M. L., et al. 2021, ApJ, 912, 10
Zajaček, M., Karas, V., & Eckart, A. 2014, A&A, 565, A17
Zhai, Z., Blanton, M., Slosar, A., & Tinker, J. 2017, ApJ, 850, 183